Rapid Mesoscale Environmental Changes Accompanying Genesis of an Unusual Tornado

STEVEN E. KOCH

NOAA/National Severe Storms Laboratory, Norman, Oklahoma

RANDOLPH WARE

Radiometrics Corporation, and National Center for Atmospheric Research, and Cooperative Institute for Research in the Environmental Sciences, Boulder, Colorado

HONGLI JIANG

NOAA/Earth System Research Laboratory, and Cooperative Institute for Research in the Atmosphere, Boulder, Colorado

YUANFU XIE

NOAA/Earth System Research Laboratory, Boulder, Colorado

ABSTRACT

This study documents a very rapid increase in convective instability, vertical wind shear, and mesoscale forcing for ascent leading to the formation of a highly unusual tornado as detected by a ground-based microwave radiometer and wind profiler, and in 1-km resolution mesoanalyses. Mesoscale forcing for the rapid development of severe convection began with the arrival of a strong upper-level jet streak with pronounced divergence in its left exit region and associated intensification of the low-level flow to the south of a pronounced warm front. The resultant increase in stretching deformation along the front occurred in association with warming immediately to its south as low-level clouds dissipated. This created a narrow ribbon of intense frontogenesis and a rapid increase in convective available potential energy (CAPE) within 75 min of tornadogenesis. The Windsor, Colorado, storm formed at the juncture of this warm frontogenesis zone and a developing dryline. Storm-relative helicity suddenly increased to large values during this pretornadic period as a midtropospheric layer of strong southeasterly winds descended to low levels. The following events also occurred simultaneously within this short period of time: a pronounced decrease in midtropospheric equivalent potential temperature θ_e accompanying the descending jet, an increase in low-level θ_e associated with the surface sensible heating, and elimination of the capping inversion and convective inhibition. The simultaneous nature of these rapid changes over such a short period of time, not fully captured in Storm Prediction Center mesoanalyses, was likely critical in generating this unusual tornadic event.

1. Introduction

Forecasting the initiation and evolution of severe local storms is challenged by the need to monitor mesoscale variability in potential instability, moisture availability, vertical wind shear, and vertical circulations at temporal and spatial scales important to nowcasting convection (Weckwerth and Parsons 2004). Nowcasting techniques for forecasting with local detail out to a few hours ahead have advanced considerably over the past couple of decades, but according to Dabberdt et al. (2005), "the full benefit of enhanced forecast model resolution has not been and will not be realized without commensurate improvements in high-resolution meteorological observations, as well as improvements in data assimilation, model physics, parameterizations, and user-specific analyses and forecast products." Indeed,

Corresponding author address: Steven E. Koch, NOAA/National Severe Storms Laboratory, 120 David L. Boren Blvd., Norman, OK 73072.
E-mail: steven.koch@noaa.gov

positive impacts of assimilating wind and thermodynamic observations from ground-based remote measurement systems have been found recently in model data sensitivity experiments (Benjamin et al. 2004; Ziegler et al. 2010; Otkin et al. 2011; Hartung et al. 2011; Illingworth et al. 2015).

The spatial and temporal scales that are most representative of the local "storm environment" are not well established. This uncertainty is reflected in the wide range of sounding proximity criteria that have been employed in previous studies, as summarized by Potvin et al. (2010). The problem is exacerbated by the fact that thunderstorms substantially modify the atmosphere immediately around them, resulting in conditions that are unrepresentative of the ambient storm environment.

The National Research Council (2009, 2010) advocated for the creation of a nationwide mesoscale network composed of ground-based sensor systems to address severe limitations in sampling the atmosphere, and recommended that profiles of wind, temperature, and moisture should extend to 3 km above ground level (AGL). In response to these reports, a comprehensive assessment of thermodynamic profiling systems for forecasting convection was conducted (Hardesty et al. 2012). For the prediction of convection initiation, strong requirements were stipulated: a time resolution of 15 min, vertical resolution of 30 m close to the surface degrading to 100 m at 3 km, horizontal resolution of at least 10 km, and bias of <5% in the lower troposphere.

The reason for such strict demands on observing systems for severe storm applications can be understood as follows. Moist boundary layer air in the central United States is often capped by a strong inversion, allowing the buildup with diurnal heating of substantial convective available potential energy (CAPE). Once the cap is broken, an explosive situation is created, and the ensuing thunderstorms may quickly become severe (thus the need for high temporal resolution). Strong horizontal gradients in water vapor ($>1\,\mathrm{g\,kg^{-1}\,km^{-1}}$) may exist across the oft-present dryline over very small distances (Ziegler et al. 1995; Buban et al. 2007). This need for very high spatial resolution also exists to monitor cross-dryline thermodynamic and kinematic fields because the dryline is typically located within a horizontal gradient of virtual potential temperature and flow deformation, which help promote frontogenesis (McCarthy and Koch 1982). Mesoscale fluctuations with spatial scales of <20 km along the dryline also can be important in convection initiation (Koch and McCarthy 1982; Atkins et al. 1998; Buban et al. 2012). Storms also frequently form at a "triple point" where

a baroclinic boundary and the dryline intersect (Weiss and Bluestein 2002; Wakimoto et al. 2006). Also, details in the vertical motion profile can impact vertical vorticity production in the presence of vertical wind shear (Wilson et al. 1998).

Supercell storms occur in environments containing substantial CAPE ($>1000\,\mathrm{J\,kg^{-1}}$) and "deep" vertical wind shear over the lowest 4–6 km AGL (Weisman and Klemp 1982; Markowski and Richardson 2010). Rasmussen and Blanchard (1998) and Weisman and Rotunno (2000) established that deep-layer shear values generally $>20\,\mathrm{m\,s^{-1}}$ are necessary for the maintenance of long-lived supercell storms. Rasmussen (2003) and Thompson et al. (2003) found that vertical wind shear and moisture within 1 km of the ground best discriminates between nontornadic and significantly tornadic supercells.

Feltz and Mecikalski (2002) found using Atmospheric Emitted Radiance Interferometer (AERI) data that large changes in the strength of the capping inversion, boundary layer moisture, and bulk atmospheric stability can occur during the few hours prior to the rapid development of severe convection. Wagner et al. (2008) found AERI-derived CAPE gradually increased to a peak roughly 1 h before a tornado or large hail forms, whereas for nontornadic storms, the CAPE was maximized considerably earlier.

Midlevel rotation can develop within the storm updraft when the storm-relative velocity is aligned with the environmental horizontal vorticity, as assessed by the storm-relative helicity (SRH; Droegemeier et al. 1993). The value of SRH has been shown in numerous studies to be one of the most useful parameters governing the likelihood of supercell storms as environments with large values of SRH (at levels ≤ 3 km AGL) support longer-lived storms than those that form in atmospheres with lesser levels of SRH (Bunkers et al. 2006). Wagner et al. (2008) showed using wind profiler data that the wind shear and SRH for both tornadic and nontornadic storms started to increase roughly 3 h before convection initiation (CI).

The above-cited studies have illustrated the value of special ground-based observations to monitor the mesoscale severe storm environment. Microwave radiometric profilers (MWRPs) and wind profilers appear to have great potential for continuous monitoring of the boundary layer with at least moderate vertical resolution even in the presence of precipitation. Ware et al. (2013) and Xu et al. (2014) showed that MWRP are even able to provide information in the presence of heavy precipitation ($>25\,\mathrm{mm\,h^{-1}}$), with the possible exception of hail. Generally, the vertical resolution of both microwave and infrared passive remote sensors is best

close to the surface and degrades rapidly with height (though less rapidly for infrared). Lidars provide higher resolution and greater accuracy than passive remote sensing systems, but as with infrared sensors, they are limited to the clear air or optically thin clouds.

MWRP and radar wind profilers have been utilized in studies of the local storm environment and mesoscale convective triggering phenomena such as cold fronts, drylines, gust fronts, bores, and gravity waves (Koch and Clark 1999; Benjamin et al. 2004; Knupp et al. 2009). These observing systems have revealed significant changes in temperature and integrated water vapor prior to CI (Güldner and Spänkuch 2001; Güldner 2013; Madhulatha et al. 2013; Ratnam et al. 2013), sometimes within only 30 min prior to CI when associated directly with a frontogenetical vertical circulation (Koch and Clark 1999). The present study demonstrates the value offered by the use of MWRP and wind profilers in capturing unusually rapid and important changes in the local environment of a strong tornado that developed near the intersection of a dryline and a warm front near Windsor, Colorado (about 80 km north of Denver), on 22 May 2008.

2. Data and methodology

Special observations available for this study included a 12-channel microwave radiometer and 404-MHz radar wind profiler to detect temporal changes in convective parameters with 5–6-min sampling. Also, a 1-km-resolution mesoanalysis and prediction system was used to relate the rapid changes detected by the profilers to the mesoscale environment of the tornado. The MWRP was located 53 km southwest of Windsor in Boulder, whereas the wind profiler was ~30 km south of Windsor at Platteville. The mesoanalysis domain and the locations of Windsor, the Boulder MWRP, the Platteville wind profiler, and the rawinsonde at the National Weather Service (NWS) office in Denver are all shown in Fig. 1a. The Windsor supercell developed very close to the Denver airport (at "R" in Fig. 1a), and the tornado touched down at 1727 UTC just 2 km from the Platteville wind profiler, damaging the profiler's data processor and other instrumentation at the site. Unfortunately, the wind profiler did not operate after 1600 UTC. The triangular area between the rawinsonde, wind profiler, and MWRP depicted in Fig. 1a will be referred to as the Windsor CI region, since this is where CI occurred.

Detailed local topography is depicted in Fig. 1b. Note in particular the location of the Palmer Lake Divide just south of Denver, an elevated plateau that is ~800–900 m higher than the surrounding region. This topographic feature has been noted in past studies to be important for CI in the Denver region and, under conditions of southerly or southeasterly flow (such as occurred in the Windsor case), the probable cause for the formation of the "Denver cyclone" (Szoke et al. 1984) within the area just downstream (northwest) of the plateau, which is in close proximity to the Windsor CI region.

a. Microwave radiometer

Microwave radiometers can obtain vertical profiles of temperature and water vapor density under most weather conditions in the lower troposphere at time intervals of a few minutes (Hardesty et al. 2012). The present study used the Radiometrics 12-channel MP-3000 (Güldner and Spänkuch 2001; Ware et al. 2003; Liljegren et al. 2004; Cimini et al. 2006, 2011). This MWRP observed brightness temperatures related to atmospheric moisture in five frequency bands from 22 to 30 GHz and temperature in seven bands from 51 to 59 GHz. Cloud-base height was automatically determined by mapping zenith infrared temperature observations from a collocated 9.6–11.5-μm radiometer, sheltered from corrosion and wetness, to the retrieved temperature profile.

To have the highest signal to noise possible while not sacrificing temporal information important to our scientific objectives, we used 5-min-averaged data, even though the sampling rate of this radiometer can be as short as 10 s. Typical RMS errors associated with temperature and humidity retrievals from this radiometer are similar to radiosonde errors: 0.6 K near the surface, increasing to 1.6 K at 7 km, and 0.25 g m^{-3} error near the surface, increasing to 0.90 g m^{-3} at 2 km, respectively (WMO 2010). The effective vertical resolution of the MP-3000 is ~50 m near the surface, degrading with height. Mixing-layer height estimates derived from MWRP brightness temperatures characteristically display 10-m mean differences and 0.8 correlation up to 3-km height in comparison with lidar mixing height estimates (Cimini et al. 2013).

The "inverse problem" in radiative transfer (determination of profiles of temperature or water vapor from multichannel radiances) is ill posed, meaning that its solution is neither unique nor stable. Accordingly, a priori knowledge of the atmospheric variable (temperature or water vapor) is needed to constrain the solution to obtain those variables from the measured brightness temperatures. A popular method, used herein, is to employ a neural network retrieval technique trained with several years of historical radiosonde soundings from a location with similar altitude and climatology to the radiometer site (Solheim et al. 1998; Ware et al. 2003; Westwater et al. 2005; Cimini
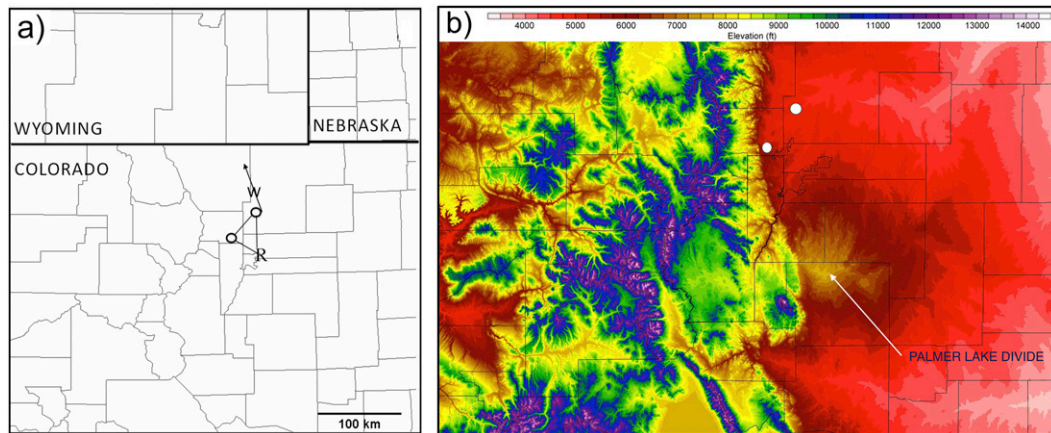
FIG. 1. (a) Map depicting the domain of the 1-km vLAPS analyses, the locations of the microwave radiometer near Boulder, the wind profiler near Platteville (the two small circles, with the profiler being the one farther northeast), the Denver NWS rawinsonde (R), and Windsor (W). The triangular area between the Denver rawinsonde, the microwave radiometer, and the wind profiler is the Windsor CI region (CI occurred at the Denver International Airport at R). Arrow indicates the general path of the Windsor tornado. The tornado touched down within 2 km of the wind profiler. (b) Color-filled topographic map of the CO portion of the vLAPS domain, depicting the Palmer Lake Divide, an elevated plateau southeast of Boulder/Denver. Locations of the radiometer and wind profiler are depicted by white dots. The Front Range is the steeply sloped terrain due west of Boulder.

et al. 2006; Knupp et al. 2009; Madhulatha et al. 2013). Alternatively, one-dimensional variational retrieval can be used with numerical weather prediction model data to obtain the thermodynamic retrievals (Hewison 2007; Cimini et al. 2011, 2013; Ware et al. 2013; Illingworth et al. 2015).

Accurate surface temperature data are needed for the radiometer retrievals. Regrettably, the MP-3000 was involved in engineering testing on the day of the Windsor tornado, so the fan that aspirated the surface temperature and relative humidity sensors on the MP-3000 was not operating to specification. Initial radiative retrievals using this surface temperature showed significant biases and unrealistic lapse rates, so we substituted the aspirated surface data from the sensor attached to a collocated, but uncalibrated 35-channel version of this instrument (the MP-3000A) for that on the MP-3000. The properly aspirated surface temperature data, along with the microwave data from the MP-3000, provided the inputs to the neural network thermodynamic retrievals.

b. Radar wind profiler

The other ground-based observing system used in this study was a NOAA wind profiler (Chadwick and Hassel 1987) operating at a frequency of 404.37 MHz. This wind profiler has a fixed phased-array, coaxial–collinear grid antenna with three beams (at zenith and two at 16.3° off-zenith). By observing refractivity gradients in the clear air, a wind profile can be obtained every 6 min except in

the presence of heavy precipitation, when the assumption of horizontal homogeneity of the wind field across the three beams may be violated (Chadwick and Hassel 1987). Radar wind profilers have been shown to be of tremendous value in forecasting the likelihood of severe convective storms (Thompson and Edwards 2000; Benjamin et al. 2004).

The NOAA wind profiler samples in two modes with differing vertical resolutions, but the data used here have a 250-m vertical resolution since no observations higher than 6 km in altitude were used. Vertical wind shear and SRH were calculated at 6-min intervals from the radial velocities, assuming horizontal homogeneity of the wind field across all beams. This assumption of homogeneity is often violated in the presence of convective precipitation, and in fact, the raw data exhibited dropouts at some of the higher data gates because of low signal to noise (Fig. 2a). To provide a continuous, uniform display of the data, the Trexler and Koch (2000) analysis technique was adapted to these data, whereby quality control procedures and a two-pass Barnes objective analysis were applied to the wind components to interpolate the data to a regularly spaced grid in order to fill small gaps in the dataset. The resulting analysis is shown in Fig. 2b.

c. Variational mesoanalysis and prediction system

A 1-km version of the variational Local Analysis and Prediction System known as vLAPS (Jiang et al. 2015) was coupled with the Advanced Research version of the
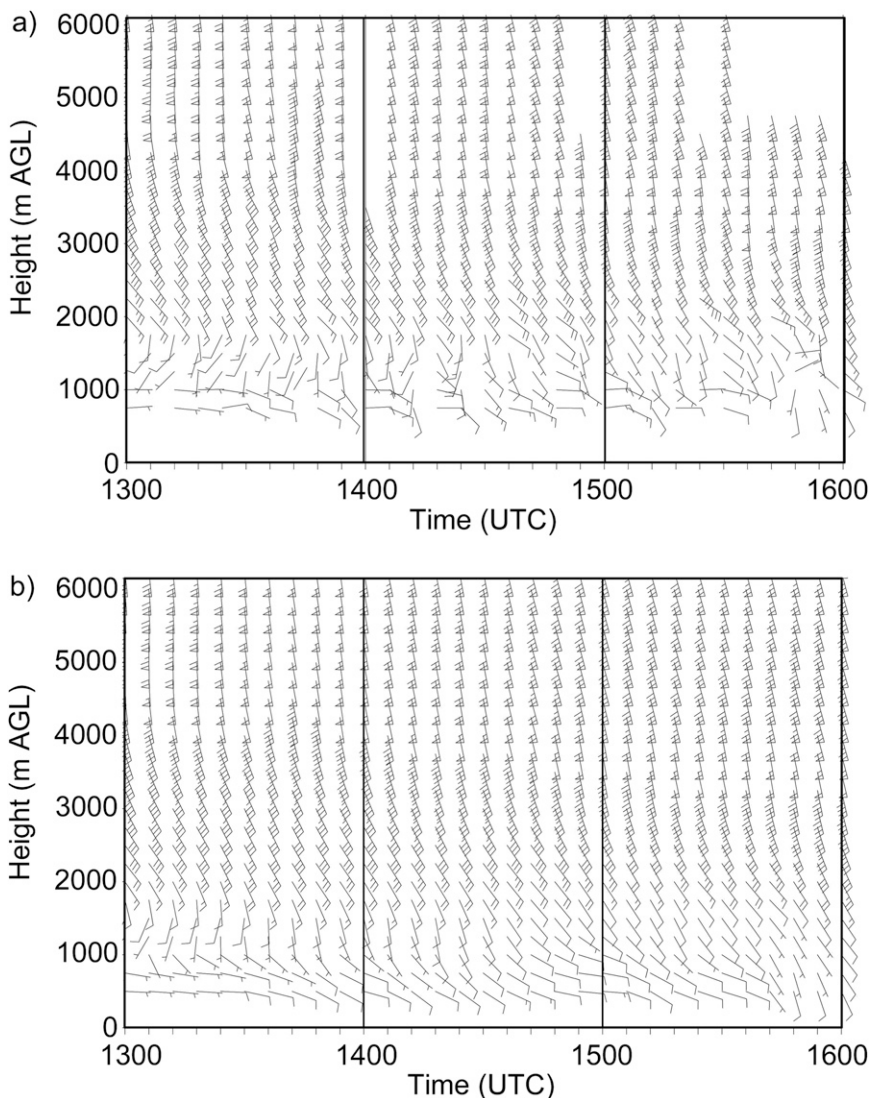
FIG. 2. Time–height display of wind profiler data (a) prior to and (b) following quality control and objective analysis (Trexler and Koch 2000). Plot shows 6-min sampled horizontal wind vectors (kt) every 250 m over the 0–6-km layer from 1300 to 1600 UTC.

Weather Research and Forecasting (WRF) Model (ARW) to relate the temporal details provided by the ground-based thermodynamic and wind profiling observations to the mesoscale environment of the tornado. Basically, vLAPS is a variational extension of the original LAPS (Albers et al. 1996; Hiemstra et al. 2006), which since its inception had used a two-pass, distance-weighting objective analysis scheme (Koch et al. 1983) with dynamic balancing. LAPS pioneered an approach called "hot start," whereby variables strongly affected by deep, moist convection such as vertical velocity, temperature, moisture, and cloud microphysical properties are analyzed and mutually adjusted to fully capture moist diabatic processes.

In the variational version of LAPS, a multigrid technique is adopted to combine the advantages of three-dimensional variational analysis and the multiscale Barnes objective analysis by solving a sequence of variational minimization problems at multiple scales (Xie et al. 2011). In the spatial domain, the largest scale features are analyzed first, followed by the addition of finer spatial scale details in successive iterations, whereas in the temporal domain, multiple time frames are analyzed in a single minimization, allowing the extraction of information from frequent observations (e.g., from radar) related to rapid changes. Verification statistics for vLAPS are described in Jiang et al. (2015).

TABLE 1. Times of data availability for the various systems used in this study. Cells denoted with "X" have data availability. The wind profiler went down at 1600 UTC, and vLAPS 1-km analyses were produced beginning at 1230 UTC. The tornado touched down within 2 km of the wind profiler at 1727 UTC.

Data availability	0000 UTC 22 May–0000 UTC 23 May 2008												
Time (UTC)	00	02	04	06	08	10	12	14	16	18	20	22	24
Microwave radiometer	X	X	X	X	X	X	X	X	X	X	X	X	X
Wind profiler	X	X	X	X	X	X	X	X					
vLAPS							X	X	X	X	X	X	X

For the current application, first-guess fields for a 3-km version of vLAPS analyses came from the 12-km resolution North American Mesoscale (NAM) model. These vLAPS analyses then provided initialization fields for the ARW to generate 3-km resolution forecasts. The model was initialized at 1200 UTC 22 May 2008, and forecasts were produced out to 0000 UTC 23 May. Finally, these 3-km WRF Model forecasts were used as the first guess (background) to create the 1-km vLAPS analyses from bilinear interpolation beginning at 1230 UTC, which are the fields shown in this paper.

Tables 1 and 2 summarize the data availability for this study. The microwave radiometer produced continuous data over the entire 24-h period, but the wind profiler produced data only until 1600 UTC. The vLAPS assimilated data from the Platteville wind profiler and Boulder radiometer, as well as several other units in the vLAPS domain; reflectivity and radial wind data from six NWS WSR-88D radars in this domain; soundings, cloud-track winds, and total precipitable water from geostationary satellites; aircraft data; ground GPS-Met sensors; and other conventional data. Only the lowest 1 (2) km of temperature (water vapor) data retrieved from the radiometer were used by vLAPS, whereas the entire 16-km depth of the wind profiler dataset was assimilated. A data impact experiment was run to test the impact of withholding the wind profiler data from the vLAPS data assimilation system. Results indicated negligible impact (e.g., wind differences in the Platteville region were all $<5\,\mathrm{m\,s^{-1}}$ at all levels from 1300 to 1800 UTC), which is not surprising given the limited spatial coverage of this profiler data. Since the results were insignificant from the wind profiler data-denial study, we did not perform a similar experiment withholding the microwave radiometer data from vLAPS.

3. Case overview

The event to be discussed herein was an [enhanced Fujita (EF) scale] EF3-rated tornado that occurred at Windsor, just before 1200 mountain daylight time (MDT; 1800 UTC) on 22 May 2008. As discussed by Schumacher et al. (2010, hereafter S10), this event was unusual for a number of reasons. First, the Front Range of the Rocky Mountains is unaccustomed to strong tornadoes, particularly ones that occur in the morning. Also, the tornado had a very uncommon track to the northwest and displayed the longest track of any recorded tornado with a westward component in this region; in fact, it is the only EF3-rated tornado ever recorded near the Front Range with such a track. S10 discussed how this event included a southerly upper-level

TABLE 2. Number of observations available by type in the 3-km vLAPS domain during the 15-min vLAPS data assimilation window. Some observation types are available at a frequency higher than the vLAPS data assimilation interval. The other two radiometers besides the one in Boulder were in the states of AL and OH, so their influence is negligible on the regional analysis. The six radars used in the remapping to the vLAPS grids were Denver (KFTG); Pueblo, CO (KPUX); Cheyenne, WY (KCYS); Goodland, KS (KGLD); Riverton, WY (KRIW); and Grand Junction, CO (KGJX). "Satellite soundings" consist of four channels from *GOES-12*: visible, water vapor, infrared window, and shortwave.

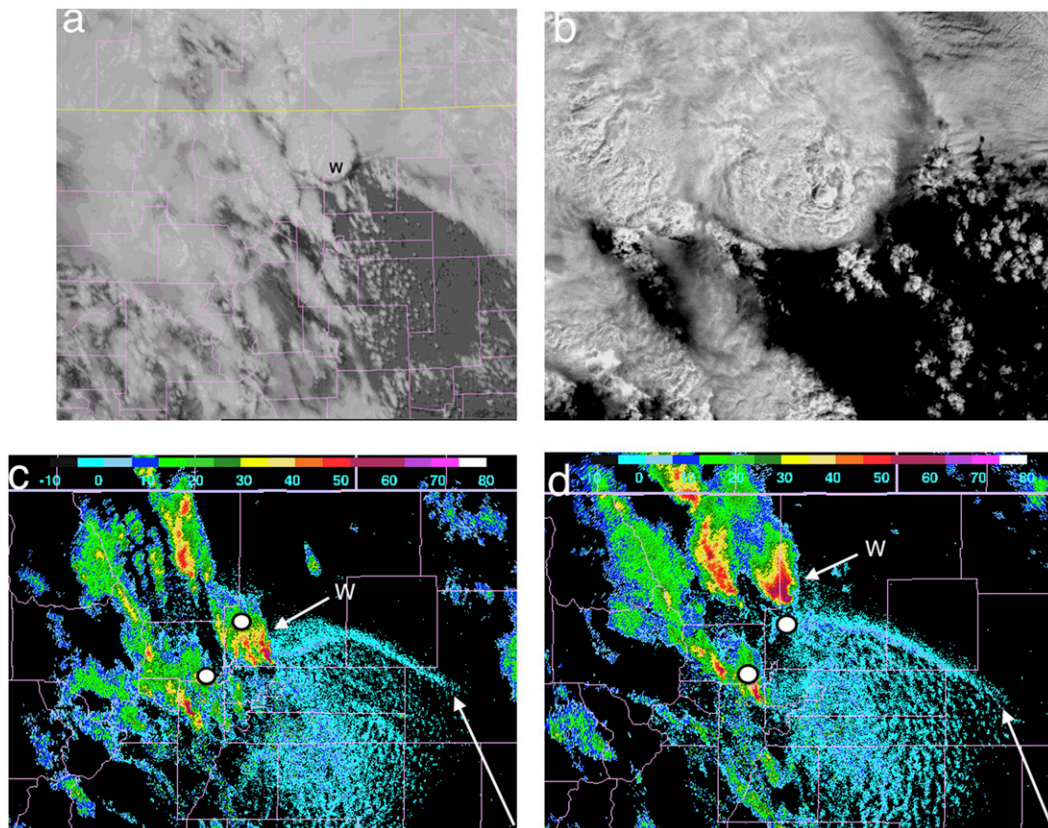| Observing systems	No. of observations types	Data frequency
Profiler	14 profilers	6 min
ACARS	127–251	Continual
Aviation routine weather report (METAR)	148–160	1 h
Radiometer	Three radiometers	1 h
Surface mesonets	2630	5–60 min
Pilot reports	5–20	Continual
Multiradar mosaic	Six radars	5 min
GOES cloud drift winds	7000	1 h
Satellite soundings	Four channels	15 min

FIG. 3. (a) GOES visible albedo satellite imagery at 1730 UTC, (b) MODIS imagery of the Windsor storm at 1800 UTC 22 May 2008, and vLAPS radar reflectivity analysis at (c) 1710 and (d) 1753 UTC. Locations of the radiometer and wind profiler (white dots) are depicted as in Fig. 1. The letter W denotes the Windsor storm. The unmarked white arrows in (c) and (d) denote the warm front "fineline."

jet streak exceeding $40\,\mathrm{m\,s^{-1}}$, a pronounced low pressure center located just east of Denver, a strengthening warm front to the east-northeast of the surface cyclone that had advanced northward the previous night in response to the approach of the upper-level trough, and a dryline that developed in late morning to its south. Dry, gusty, southerly winds materialized to the southwest of the dryline, while southeasterly winds advected warm, moist air to its east and cool, easterly flow conditions prevailed north of the warm front.

S10 estimated mixed-layer CAPE (MLCAPE) values > $2000\,\mathrm{J\,kg^{-1}}$ and storm-relative helicity in the 0–1-km layer of $219\,\mathrm{m^2\,s^{-2}}$ using a Denver 1800 UTC sounding (released ~100 km to the south of the warm front) that was subjectively modified to account for the cooler, moister surface conditions in the local vicinity of Windsor. These instability and helicity values are consistent with supercell thunderstorm environments (Thompson et al. 2003). The lifting condensation level was only ~1.0 km AGL for the cloud-covered region just north of the warm front, which is unusually low for eastern Colorado (Thompson et al. 2013). Thus, the air entering the Windsor storm at cloud base was exceedingly moist, unstable, and had plentiful vertical wind shear.

Low-level clouds immediately to the south of the warm front in the vicinity of the radiometer and profiler dissipated by 1600 UTC, allowing substantial solar radiation to warm the surface. The warm front at 1730 UTC was located along the southern edge of a northwest–southeast-oriented band of low clouds southeast of the storm "W" (Fig. 3a). From the vLAPS radar analysis perspective, the warm front appears as an arc of low reflectivity stretching east-southeast of the storm (long arrows in Figs. 3c,d). The unusual location and orientation of the "hook echo" in Fig. 3d, being located on the southeastern side of the storm and turned 90° counterclockwise from a normal alignment, are due to the fact that the storm motion was northwesterly. The crisp anvil edge to the cumulonimbus cloud on its southeastern side (Fig. 3b) reveals that the deep-tropospheric wind shear was from the south-southeast.
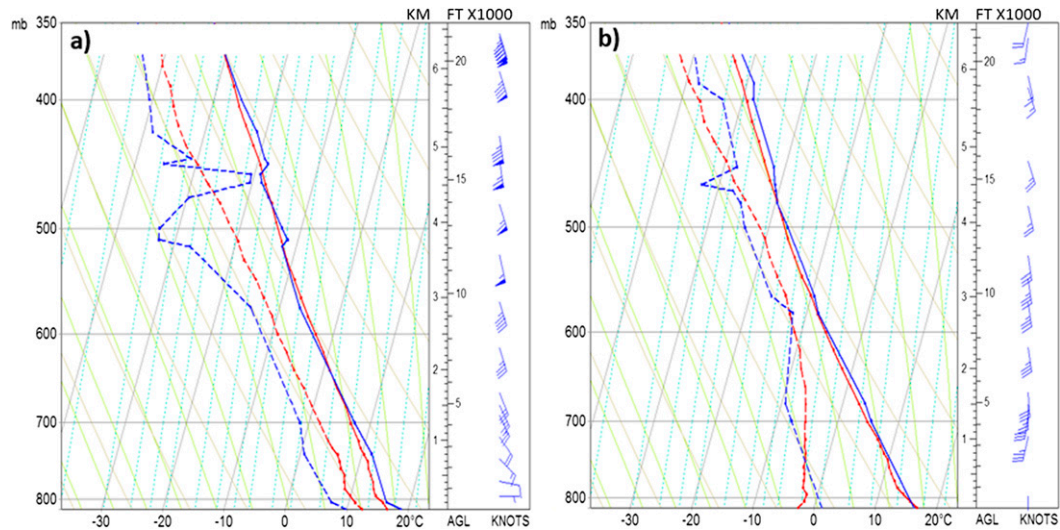
FIG. 4. Skew-T plots comparing radiometer thermodynamic retrievals (red lines) to NWS Denver (KDNR) soundings (blue lines) at (a) 1800 UTC 22 May and (b) 0000 UTC 23 May. Retrievals are based on the 12-channel version of the radiometer upon replacing the surface temperature data with that from the 35-channel version, as discussed in the text. Solid lines show temperature; dashed lines depict the dewpoint temperature. Displayed winds (kt) are from KDNR.

Initial convection developed at ~1630 UTC close to the Denver International Airport along the warm front where it intersected a developing dryline (Finch and Bikos 2010). The first severe thunderstorm warning was issued at 1709 UTC and was followed by a tornado warning 9 min later. Tornado touchdown was reported at 1727 UTC ~25 km southeast of Windsor, just 2 km from the location of the Platteville wind profiler. The storm that produced this large tornado was a long-lived supercell (Bunkers et al. 2006) that later produced a second tornado in southern Wyoming, the subject of studies by Finch and Bikos (2010) and Geerts et al. (2009).

4. Analysis of the mesoscale environment

The results of the analyses of the radiometer and wind profiler data are discussed in section 5. It is helpful to understand these detailed observations within the context of the local mesoscale environment of the Windsor storm, so we address this matter next.

a. Local thermodynamic and wind shear environment

Profiles of thermodynamic retrievals from the 12-channel MWRP are compared to the NWS Denver rawinsondes at 1800 UTC 22 May and 0000 UTC 23 May in Figs. 4a and 4b, respectively. The temperature profiles from the MWRP are in excellent agreement with those measured by the two rawinsondes throughout the entire atmosphere below the tropopause (350 hPa), though for

reasons discussed earlier, weak midtropospheric inversions are not detected by the radiometer. The water vapor profiles at 0000 UTC are in overall good agreement, but there are systematic differences in the moisture profiles between the radiosonde and radiometer (which displays higher humidity) at 1800 UTC. This difference is real; it reflects the large contrast in moisture across the warm front, with the radiometer being located in the vicinity of deep clouds on the north side of the front, and the drier Denver radiosonde being taken within mostly sunny conditions to its south (Fig. 3a). In fact, this disparity disappears 6 h later, by which time the dryline had passed through the entire Denver–Windsor area. Time series of cloud-base levels measured by the MP-3000A infrared sensor (not shown) indicated that cloud bases descended to the surface in the predawn hours and continued through 1600 UTC, and that considerable variability in cloud-base heights existed for the next 2 h as the radiometer sensed a mix of decreasing stratus clouds and developing cumulus congestus clouds with somewhat higher cloud bases. This is consistent with the available surface reports and satellite imagery.

A sample radiometer-derived sounding for 1706 UTC (Fig. 5), selected because it was the time at which the radiometer exhibited the highest value of surface-based CAPE (SBCAPE), shows a substantial amount of "positive area" for a parcel lifted from the surface. The combination of $30 \, \text{m s}^{-1}$ of vertical wind shear in the 0–4-km AGL layer (from the Denver sounding) and SBCAPE of $2866 \, \text{J kg}^{-1}$ (from the radiometer) are
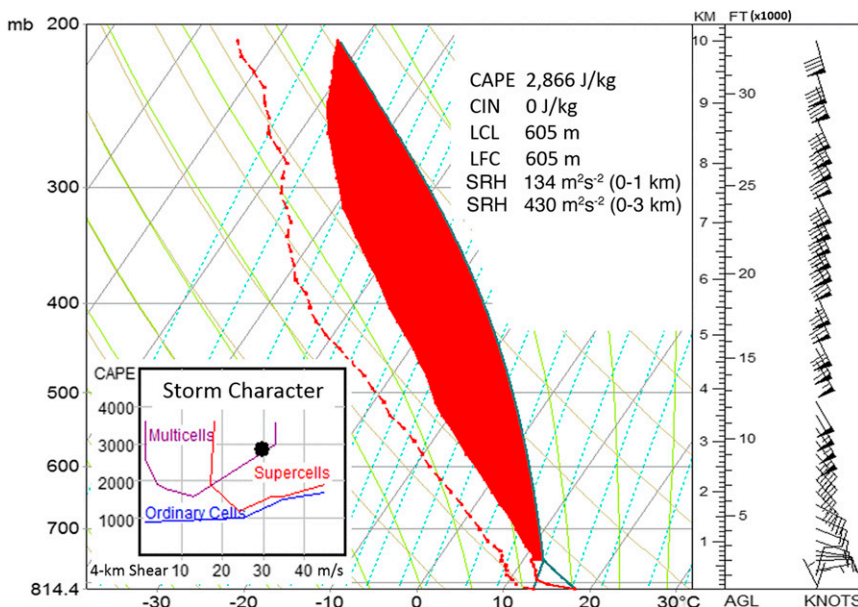
FIG. 5. Radiometer-derived sounding at 1706 UTC showing the lifted parcel positive area (red) to the right of the temperature profile. The computed LCL of 605 m matches the LFC; thus, there was no convective inhibition (CIN = 0). Winds are taken from the 1800 UTC Denver rawinsonde. Inset shows that the combination of 0–4-km wind shear ($30\,\mathrm{m\,s^{-1}}$) and SBCAPE ($2866\,\mathrm{J\,kg^{-1}}$) classifies this sounding as being indicative of supercell storm character. SRH is 134 (430) $\mathrm{m^2\,s^{-2}}$ in the 0–1- (0–3-) km layer. This plot and Figs. 4, 10, and 11 were produced by the raob analysis and display software system (www.raob.com).

indicative of a supercell environment (Rasmussen and Blanchard 1998; Weisman and Rotunno 2000; Thompson et al. 2003; Markowski and Richardson 2010). The lifting condensation level (LCL) of 605 m AGL matches the level of free convection (LFC); that is, no convective inhibition (CIN) existed at this time.

The wind profile in Fig. 5 obtained from the 1800 UTC Denver rawinsonde shows strong veering of the winds from an easterly direction in the lowest 1 km AGL to 55 kt ($28\,\mathrm{m\,s^{-1}}$; 1 kt = $0.51\,\mathrm{m\,s^{-1}}$) SSE at 3 km AGL. SRH was calculated from this sounding for the 0–3- and 0–1-km AGL layers. Rasmussen (2003, hereafter R03), found that differences between significantly tornadic and nontornadic supercells are most pronounced using the lowest 1-km layer ($\mathrm{SRH_{0-1}}$). Our calculation revealed $\mathrm{SRH_{0-1}}$ and $\mathrm{SRH_{0-3}}$ values of 134 and $430\,\mathrm{m^2\,s^{-2}}$ in the 0–1- and 0–3-km AGL layers, respectively. The latter value is far in excess of the minimum criterion ($150\,\mathrm{m^2\,s^{-2}}$) Markowski and Richardson (2010) suggested as indicating supercell potential. The value of $\mathrm{SRH_{0-1}}$ agrees well with the value of $100\,\mathrm{m^2\,s^{-2}}$ seen in the Storm Prediction Center (SPC) mesoanalysis at 1800 UTC (http://www.spc.noaa.gov/exper/mesoanalysis/archive). The combination of an LCL height of 605 m AGL and a 0–1-km shear value of $12\,\mathrm{m\,s^{-1}}$ places the 1800 UTC Denver sounding in the

tornadic supercell category of Craven and Brooks (2004). The combination of radiometer-measured SBCAPE = $2866\,\mathrm{J\,kg^{-1}}$ and rawinsonde $\mathrm{SRH_{0-1}} = 134\,\mathrm{m^2\,s^{-2}}$ (which, as shown below, is in excellent agreement with the vLAPS analyses) results in an "energy–helicity index" (EHI) of 2.4, a value that exceeds the median value of EHI for significantly tornadic storms (Thompson et al. 2003).

b. Mesoscale environmental forcing of convection

The vLAPS analyses produced every 15 min on a 1-km grid were used for diagnostic examination of the near- and prestorm environment over the domain shown in Fig. 1a. The context for this discussion begins at the 300-hPa level, as a strong ($>50\,\mathrm{m\,s^{-1}}$) upper-level jet (ULJ) streak approached the Windsor CI region (Fig. 1a) from the south. With the approach of the ULJ streak, and just before deep convection broke out, winds backed from southerly at 1400 UTC to southeasterly by 1630 UTC (Fig. 6) in the left-exit region of the ULJ streak located over the Rocky Mountains west of the Windsor CI region. This resulted in a mesoscale region of pronounced diffluence (highlighted by the arrow in Fig. 6b) immediately to the southwest of this area.

To determine whether this diffluence was associated with divergence, the vLAPS 1-km resolution analyses
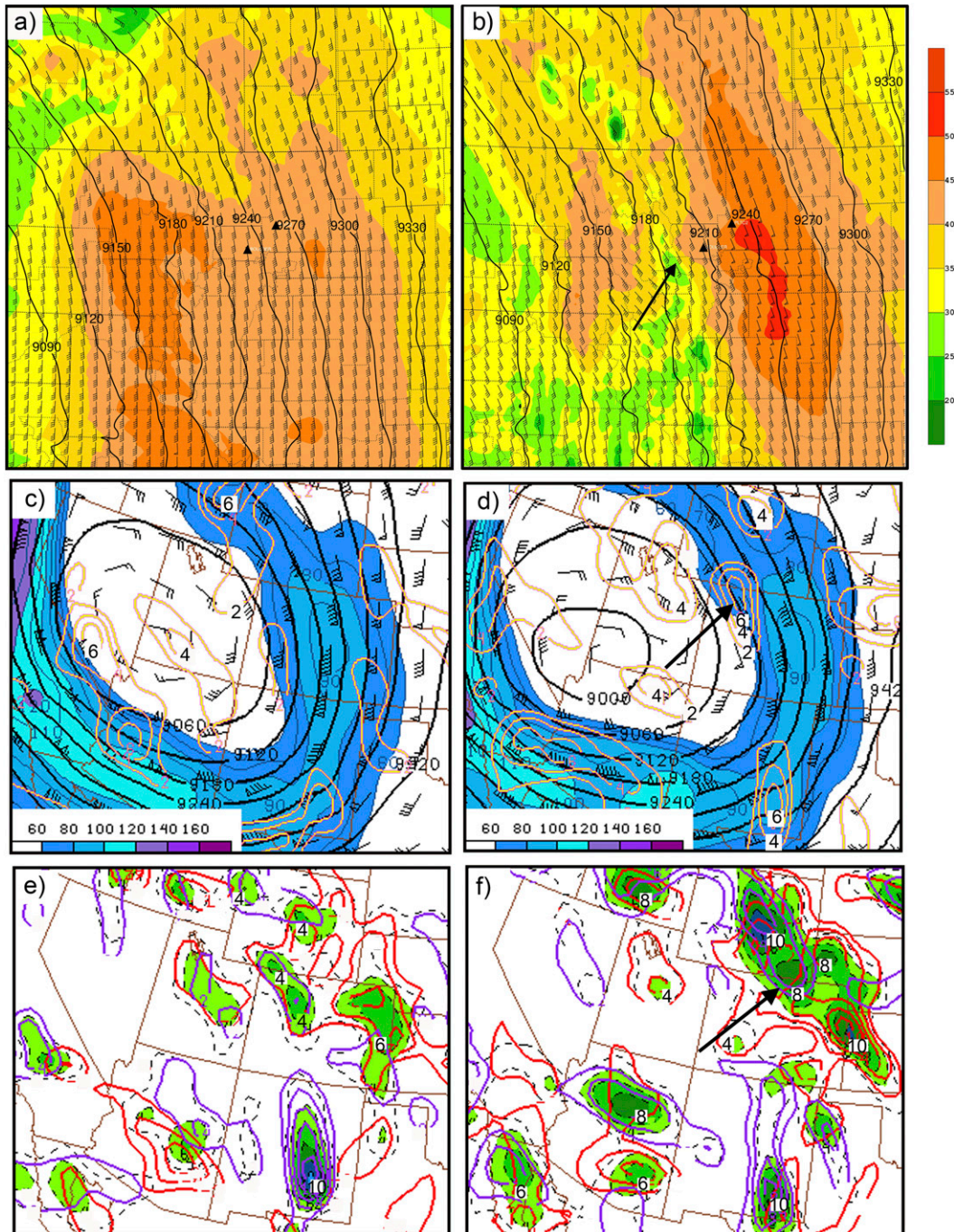
FIG. 6. (a) Wind vectors (m s^{-1}), color-filled isotachs (m s^{-1}), and geopotential heights (30-m intervals) at 300 hPa from 1-km vLAPS analyses over the domain shown in Fig. 1a at 1400 UTC. (b) As in (a), but at 1630 UTC. Locations of the microwave radiometer and wind profiler are depicted by small triangles. Arrow in (b) points to the mesoscale region of increasing diffluence that develops to the immediate southwest of these instruments in association with northward propagation of the 50+ m s^{-1} jet streak. Larger-scale analyses from the SPC mesoanalysis are shown: (c),(d) 300-hPa wind vectors (kt), color-filled isotachs (20-kt intervals), divergence (2 × 10^{-5} s^{-1} intervals), and geopotential heights (60-m intervals) at 1400 and 1700 UTC, respectively, and (e),(f) 250-hPa divergence (purple; 2 × 10^{-5} s^{-1} intervals), 850-hPa convergence (red; 2 × 10^{-5} s^{-1} intervals), and 250–850-hPa differential divergence (color fill, 2 × 10^{-5} s^{-1}). Arrows in (d) and (f) point to areas of particular interest described in the text.

were further diagnosed. The results (not shown) did reveal a substantial increase in the 300-hPa divergence from 1400 to 1630 UTC, but terrain circulations masked the background subsynoptic divergence field associated with the jet streak. Since a coarser-resolution analysis was required to detect the subsynoptic signature associated with the jet streak, we employed the 40-km-resolution SPC mesoanalyses, which utilized Rapid Update Cycle (RUC-2) initial fields modified with a two-pass Barnes analysis (Koch et al. 1983) of surface observations available near the top of each hour. The divergence field at 300 hPa for 1400 and 1700 UTC is shown superimposed upon the isotach and geopotential height fields in Figs. 6c and 6d, respectively. A sizable increase in divergence developed over northwestern Colorado in the left-exit region of the ULJ (the arrow points to this feature), but displaced slightly westward of where the strongest diffluence is evident in the vLAPS analyses. The differential divergence between 250 and 850 hPa (i.e., the divergence at 250 hPa minus that at 850 hPa) is shown in Figs. 6e and 6f for these same two times. This field is shown because it provides a clearer picture of the deep-tropospheric transverse vertical circulation associated with the ULJ. A pronounced increase in net divergence is seen to have occurred across northern Colorado and southeastern Wyoming along an axis stretching from central Wyoming to far eastern Colorado.

A surface low pressure system and associated cyclonic circulation were present throughout the morning of 22 May 2008 immediately downstream (northwest) of the Palmer Lake Divide (Fig. 7), a configuration that is quite characteristic of the Denver Cyclone (Szoke et al. 1984). With the approach of the ULJ streak, the surface cyclonic circulation and southeasterly surface winds to the south of the warm front strengthened and, accordingly, so did the stretching deformation along the warm front. The combination of the increasing deformation with the sensible heating that commenced as the low-level clouds to the south of the warm front broke up caused a sizable increase in the cross-frontal temperature gradient (Fig. 7d).

Close inspection of these fields shows that the center of the cyclone retrograded slightly westward from 1400 to 1730 UTC. The preexisting pool of moisture $> 9\,\mathrm{g\,kg^{-1}}$ near the warm front at 1400 UTC responded by arcing southwestward toward the southern perimeter of the Windsor CI region by 1730 UTC (Fig. 7e). The combination of ample moisture and increasing deformation along the warm front, with intensification of the southeasterly flow and substantial surface heating south of the front, resulted in a narrow, arc-shaped ribbon of anomalously high equivalent potential temperature

$(\theta_e > 336\,\mathrm{K})$ directed right at the southeast corner of the Windsor CI region at the time of tornadogenesis (Fig. 7f). Also note the intensification of the dryline as southerly winds crossed the Palmer Lake Divide and flowed downslope to create drier conditions just to the south of Denver, in association with increased vertical mixing that arose with the late-morning sensible heating. The Windsor supercell storm formed in this localized θ_e "hot spot" of 342 K at the southeast corner of the Windsor CI region, which is also near to where the dryline intersected the warm front.

Analyses of SBCAPE and the scalar frontogenetical function at the 800-hPa level (representing mean conditions throughout the lowest $\sim$100 m of the atmosphere) are shown in Fig. 8 at 1400 and 1730 UTC. During this 3.5-h period, the SBCAPE field increased from 2400 to 3000 J kg^{-1} along the southeastern edge of the Windsor CI region in close proximity to the high-θ_e anomaly. Also evident is the rapid development of an extremely narrow, sinewy band of strong frontogenesis along the warm front closely aligned with the maximum in θ_e. Its narrowness attests to the rapid increase in deformation forcing and the cross-front temperature gradient discussed above.

A primary purpose of this study is to determine the added value of special observations (the microwave radiometer and wind profiler) and very high-resolution mesoanalyses beyond what is operationally available to understand the local severe storm environment. Therefore, we compared the 1-km vLAPS analyses with the 40-km SPC mesoanalyses. Surface mixing ratio, potential temperature, and equivalent potential temperature from the SPC mesoanalyses are displayed at 1400 and 1700 UTC in Figs. 9a–d. Comparison of these fields with those from vLAPS at 1400 and 1730 UTC (Figs. 7 and 8) reveals much similarity in the general features, though important details differ. Both analyses show warming occurred south of the warm front, but this is much more pronounced in the vLAPS analyses (warming of 15°C versus only 6°C), resulting in a considerably stronger cross-front temperature gradient (and, importantly, implied frontogenesis). Ample low-level moisture $(>11\,\mathrm{g\,kg^{-1}})$ exists in both analyses, but the SPC analysis does not show the southwestward arcing of moisture toward the Windsor CI region nearly as clearly as do the vLAPS fields at 1730 UTC. The θ_e fields are also generally similar, including the maximum value of $\sim$342 K in the same location; however, the narrow ribbon of increasing θ_e in late morning is much more obvious in the vLAPS analysis, and in fact, θ_e decreases with time in the SPC fields.

Likewise, the instability fields, while similar in general appearance, are noticeably different in terms of their
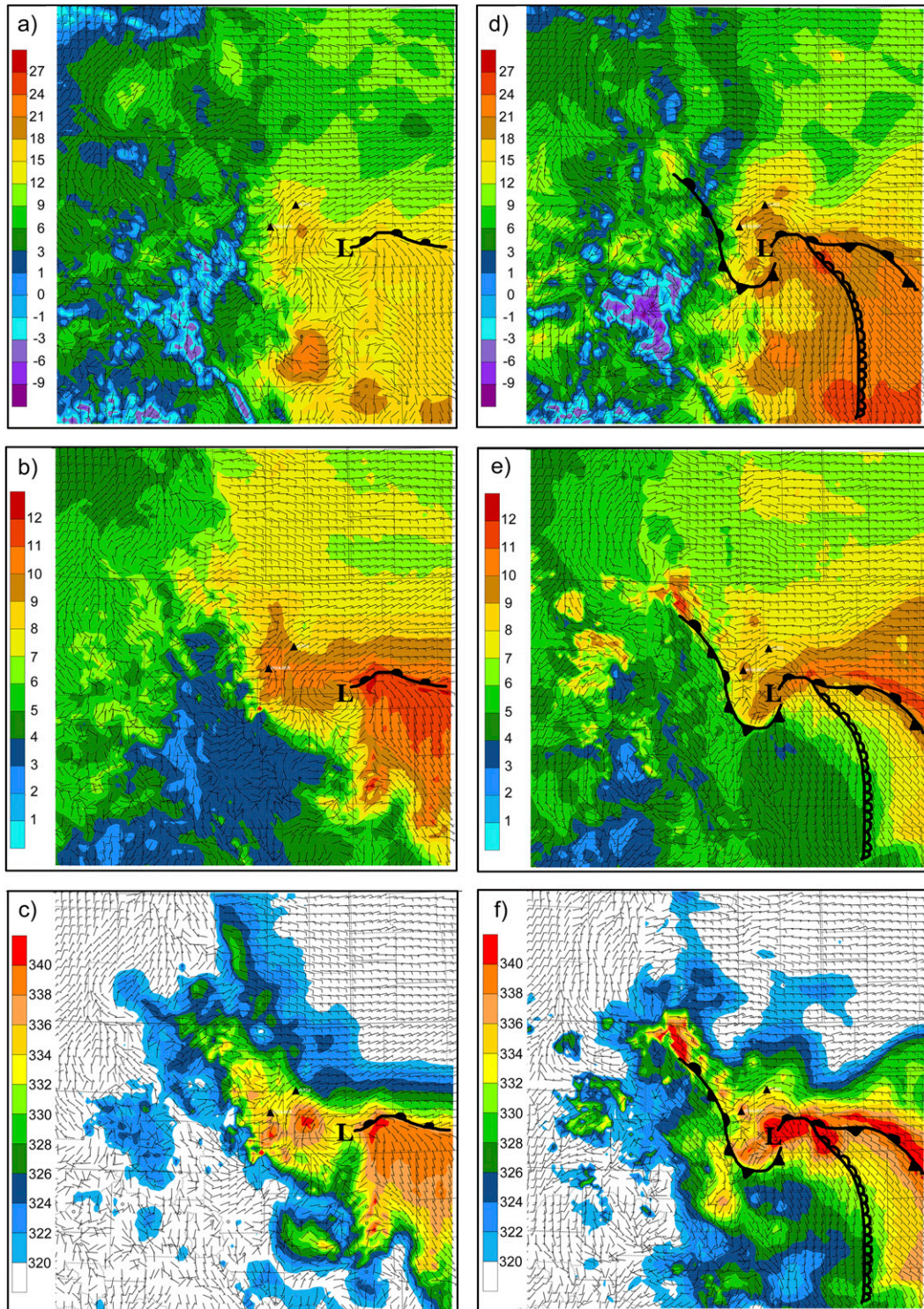
FIG. 7. The 1-km resolution surface vLAPS analyses at (left) 1400 and (right) 1730 UTC of (a),(d) temperature (°C); (b),(e) mixing ratio (g kg^{-1}); and (c),(f) θ_e (K). Winds (m s^{-1}) are depicted in all panels. Locations of the microwave radiometer and wind profiler are shown by small triangles. Denver cyclone is depicted by L.
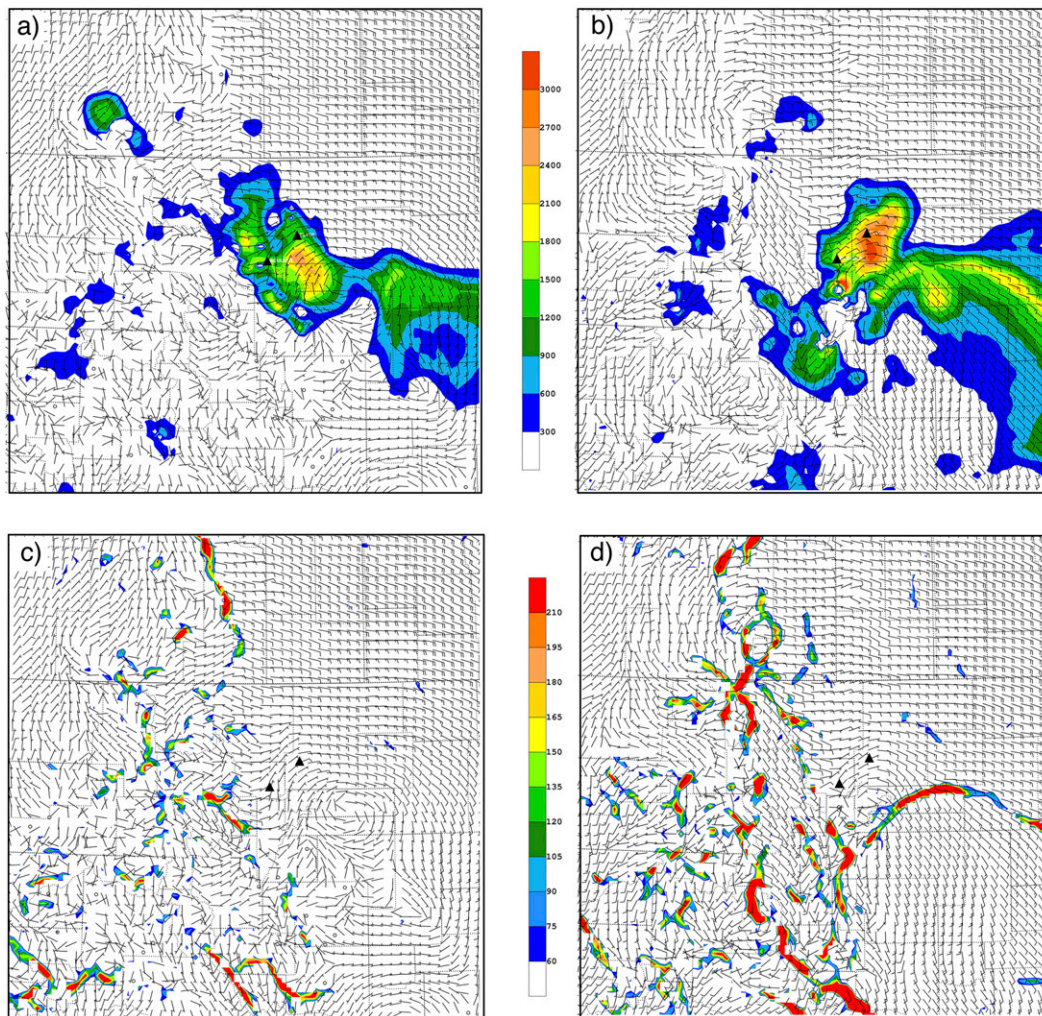
FIG. 8. As in Fig. 7, but for (a),(b) SBCAPE (J kg^{-1}) and (c),(d) frontogenesis function [°C (100 km)$^{-1}$ (3 h)$^{-1}$] and winds (m s^{-1}) at the 800-hPa level ($\sim$100 m AGL).

temporal tendencies (SBCAPE and SBCIN, and MLCAPE[1] and MLCIN from SPC are shown in Figs. 9e–h). Whereas the vLAPS SBCAPE fields (Figs. 8a,b) depict destabilization (increasing from 2400 to 3000 J kg^{-1} at the southeast corner of the Windsor CI region), the corresponding SPC meso-analyses indicate weakening instability with time, as the maximum SBCAPE decreases from $\sim$2000 to 1500 J kg^{-1}. The same general tendency is obvious in the MLCAPE fields (decreasing from 1500 to 1000 J kg^{-1} over this 3.5-h period).

In general, the vLAPS and SPC mesoanalyses both indicated a near-storm environment supportive of supercells and tornadoes. However, not only were there important differences in the details as just discussed, but as shown next, the unique observations from the microwave radiometer and wind profiler indicated very rapid changes in moisture, SBCAPE, and storm-relative helicity in the hour or so prior to the formation of the tornadic supercell that were not captured in the SPC mesoanalyses.

5. Microwave radiometer and merged wind profiler–vLAPS analyses

The Windsor tornado occurred in very close proximity to the warm front within strong horizontal gradients of moisture, CAPE, θ_e, and low-level wind shear. The

---

[1] MLCAPE was calculated here and in the radiometer analysis (Fig. 12) using the virtual potential temperature of a parcel from the lowest 1500 m of the atmosphere lifted adiabatically to the LCL and then moist adiabatically above that level.
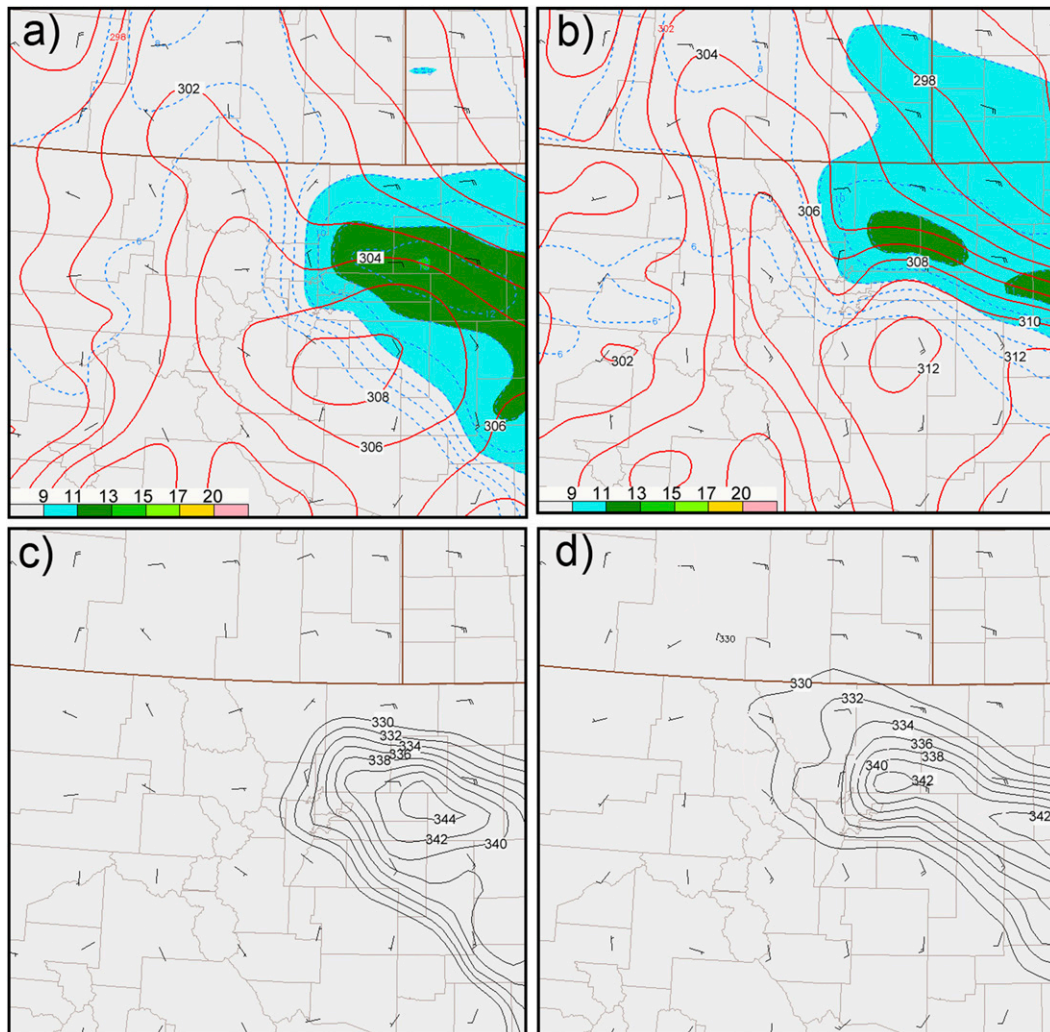
FIG. 9. SPC mesoanalyses at 40-km resolution at (left) 1400 and (right) 1700 UTC of (a),(b) surface mixing ratio (dashed lines and shaded; g kg^{-1}) and potential temperature (2-K contours) and (c),(d) surface θ_e (2-K contours).

radiometer at Boulder and the Platteville wind profiler were located 53 km southwest and 30 km to the south of Windsor, respectively. When interpreting the results from these two ground-based remote sensing systems, these distances from the Windsor tornado should be kept in mind.

a. Radiometer-derived thermodynamics

The radiometer provided excellent temporal and vertical continuity in retrieved water vapor mixing ratio and θ_e over the altitude range from the surface to 5 km AGL (Figs. 10a,b). A number of significant features of interest can be seen in this 24-h overview display. The sudden increase in the depth and magnitude of water vapor at 0530 UTC reflects the passage of the warm front over the region the night before the tornado outbreak. The radiometer reveals that the depth of this

layer of rich moisture > 9 g kg^{-1} increased for the next few hours, but then remained relatively constant until a near-surface increase occurred just before the tornado (1727 UTC). Dryline passage occurred at 1815 UTC, causing a sudden drastic reduction in moisture content and θ_e.

Of particular interest is the pronounced increase in moisture and θ_e appearing from 1630 to 1800 UTC below 1 km AGL. This sudden surge also occurred in association with rapid destabilization, as may be inferred from the rapid decrease of θ_e with height in this layer after 1700 UTC (Fig. 10b). A better depiction of this lower-tropospheric process is provided in Fig. 11, which displays the temporal variation of θ_e and potential instability (decrease of θ_e with height, i.e., a negative θ_e gradient) derived from the radiometer in the 1000-m layer immediately above the ground. This analysis reveals that extremely
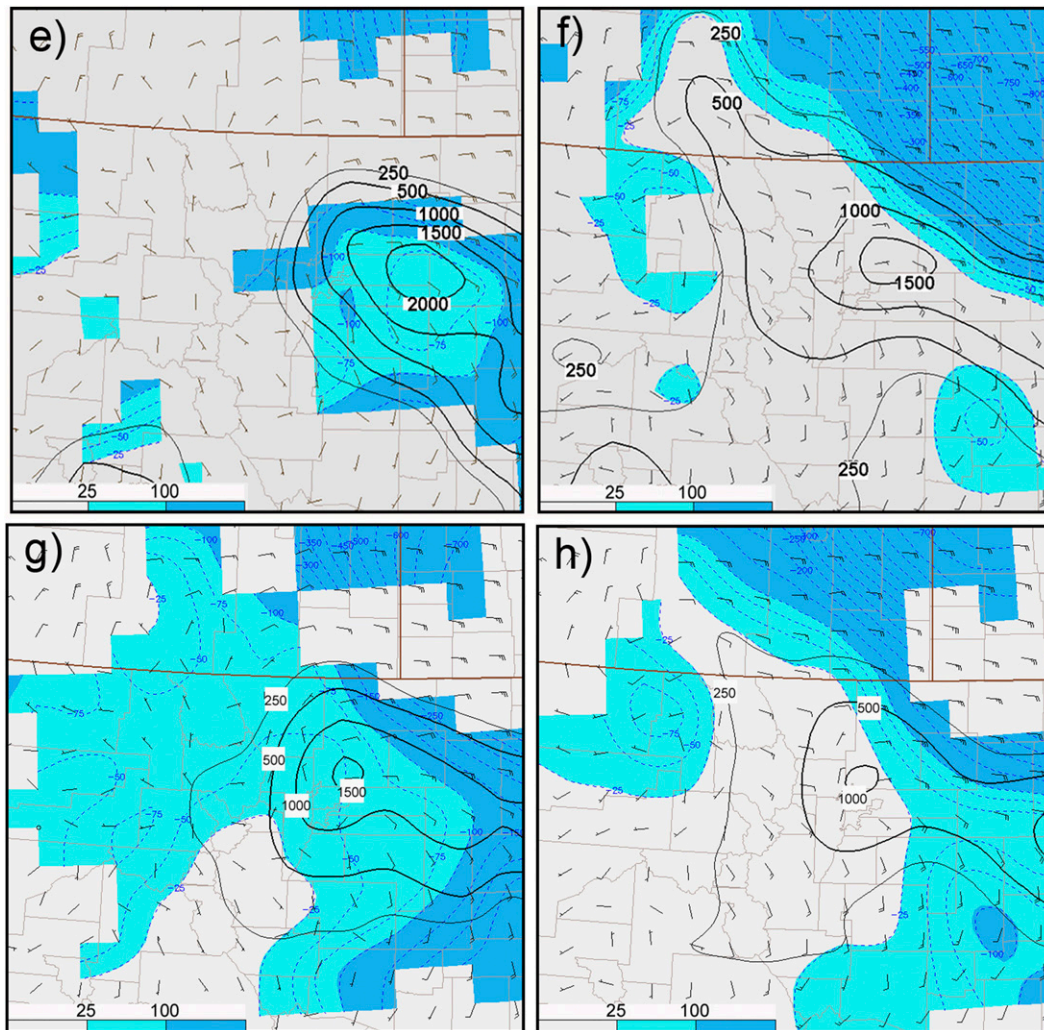
FIG. 9. (continued). (e),(f) SBCAPE (J kg^{-1}, solid lines) and SBCIN (dashed lines) and (g),(h) MLCAPE and MLCIN. CIN values greater than 25 and 100 J kg^{-1} are depicted by light and darker blue shading in all panels. Winds shown in all panels are in knots (full barb = 5 m s^{-1}, half barb = 2.5 m s^{-1}).

rapid destabilization occurred in a shallow layer within 300 m of the surface, beginning at 1630 UTC and ending at 1800 UTC, being most pronounced near the time of the nearby tornado passage. These analyses were compared to the radiometer liquid water time–height data (Campos et al. 2014; Serke et al. 2014) and satellite imagery sequences (as in Fig. 3a). That intercomparison revealed that the cause of this destabilization was due in part to the breakup of clouds in the Windsor CI region at this time, allowing solar heating to warm the surface layer and create superadiabatic conditions, but it also is attributable to low-level moistening (Fig. 10a). Closer inspection reveals an elevated layer at ~200 m AGL of strong, localized instability that first appeared 2 h earlier (at 1430 UTC). This feature is traceable to a transient dip in the θ_e isosurfaces over a rather deep layer extending to above 600 hPa (Fig. 10b).

This combination of surface-based and lower-tropospheric destabilization processes resulted in an extremely rapid increase in radiometer-based SBCAPE in a period of just 45 min prior to the tornado, reaching a peak at 1706 UTC of 2866 J kg^{-1} (2550 in 5-min averaged data; Fig. 12a) just 20 min before the tornado made its appearance. During the earlier period when θ_e and CAPE were gradually increasing (1200–1600 UTC), CIN was also continually declining, and reached essentially zero values minutes before the jump in SBCAPE commenced (Fig. 12b). The combination of essentially no inhibition to air parcels reaching their level of free convection (Figs. 5 and 12b) and abundant SBCAPE (Fig. 12a) is consistent with the explosive nature of the convective initiation commencing at 1645 UTC.
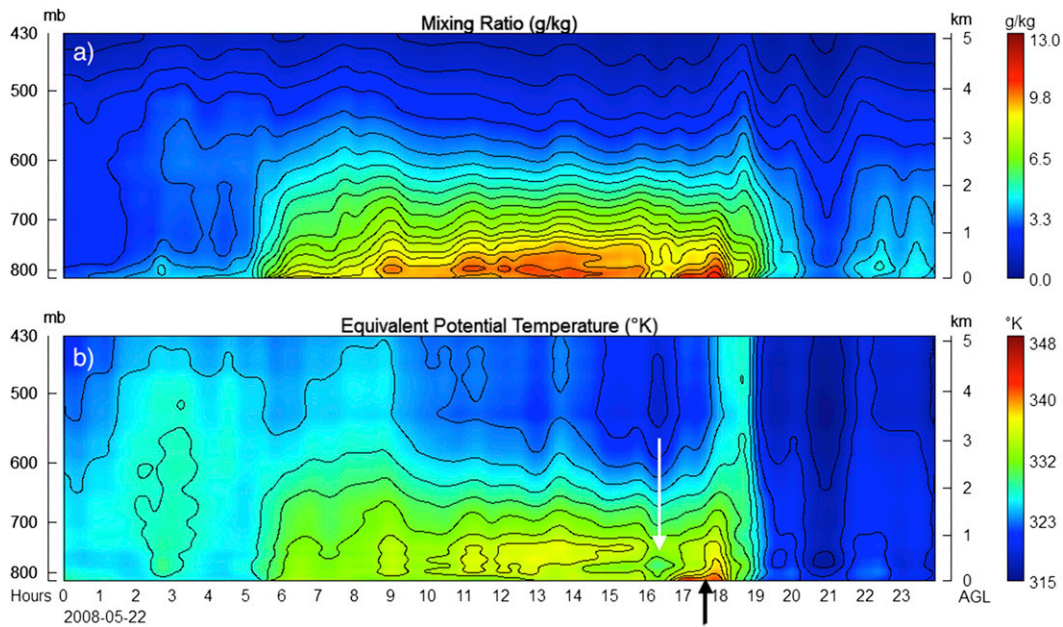
FIG. 10. Time–height 24-h display beginning at 0000 UTC 22 May 2008 of (a) water vapor mixing ratio (g kg^{-1}) and (b) θ_e (K) over the altitude range from the surface to 5 km AGL derived from the MP-3000 radiometer. Tornado touchdown occurred near the Platteville wind profiler site (47 km northeast of the radiometer) at 1727 UTC at the time of occurrence of pronounced low-level moistening and destabilization (black arrow). Dryline passed over the radiometer at 1815 UTC. White arrow denotes the deep layer of destabilization resulting from mid- to-lower tropospheric decreases in θ_e.

Comparison of surface-based and mixed-layer MLCAPE (the red line in Fig. 12a) indicates that the exceedingly rapid destabilization was confined to a very shallow layer, an interpretation consistent with the θ_e time–height data (Fig. 11). While MLCAPE is often favored among severe weather forecasters because it accounts for parcel mixing through a layer of appreciable moisture stratification, when conditions suddenly become superadiabatic and CIN disappears, as happened in the Windsor environment between 1615 UTC and tornado development, SBCAPE may be the more germane parameter to consider. We also note that since the radiometer was located in Boulder, it did not even sample the most unstable air ($>$3000 J kg^{-1}), which the vLAPS analysis (Fig. 8b) showed was located over the southern part of the Windsor CI region.

b. Wind shear and helicity analysis from merged wind profiler and vLAPS data

Since wind profiler data were unavailable after 1600 UTC, this necessitated a combined use of the profiler and vLAPS datasets to understand the evolution of the local wind shear environment. Following application of the wind profiler analysis procedures discussed in section 2b, the time–height analysis of profiler-derived horizontal winds was directly merged with wind profiles obtained from vLAPS at the grid point closest to Platteville. The resulting merged analysis (Fig. 13) shows no indication of an abrupt discontinuity at the merger time (1600 UTC), lending support to the legitimacy of the simple merger technique.

Several important inferences can be drawn from this analysis. In a general sense, vertical wind shear increases over time as the ULJ was approaching, both in terms of speed (note the descent of the 50-kt isotach) and direction (note that the winds, especially at midlevels, back from moderate southerly to strong southeasterly with time). At low levels, the presence of easterlies after 1000 UTC is associated with formation of the warm front just to the south of Platteville. The fact that this wind shift occurred 5 h after the first abrupt increase in low-level moisture detected by the radiometer (Fig. 10a) suggests that the warm front developed in stages. In fact, a closer inspection of the radiometer mixing ratio analysis indicates a secondary moisture surge at 0900 UTC, which corresponds well with this wind shift.

These pronounced changes had decided effects upon the wind hodographs determined from the merged analysis at Platteville (Fig. 14). The most important aspects of the evolving hodographs are appreciable increases in the depth and intensity of southeasterly winds in the 2–4-km layer (cf. the 1730 UTC hodograph to the
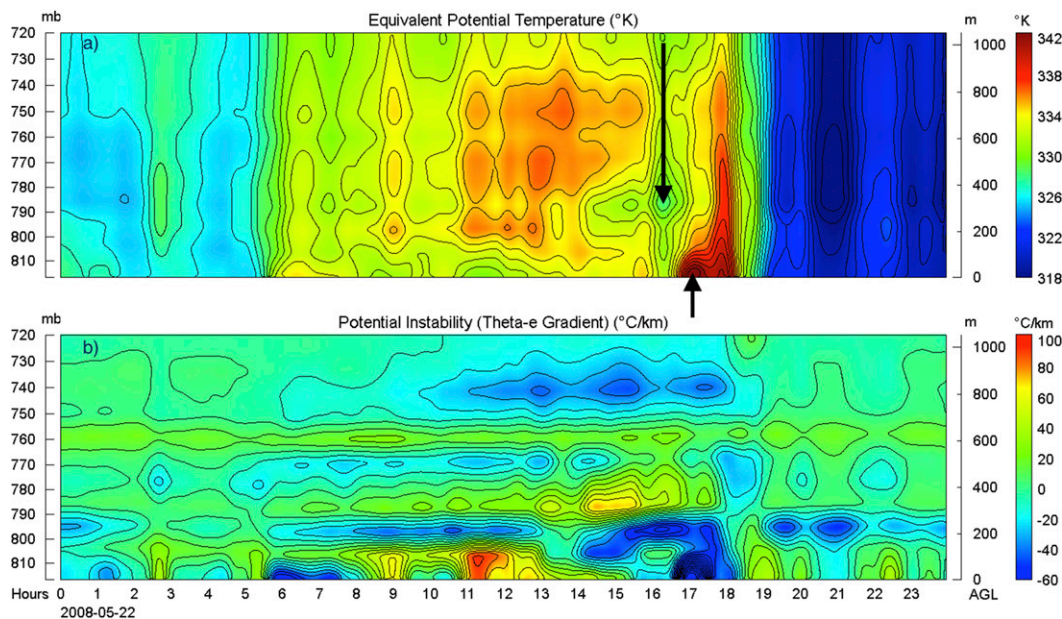
FIG. 11. Radiometer-derived variation over a 24-h period ending at 0000 UTC 23 May of (a) θ_e and (b) potential instability (K km^{-1}) calculated from the vertical gradient of θ_e within the 1000-m layer immediately above the ground. Note the rapid destabilization in the lowest 200 m after 1600 UTC with a strong maximum near the time of nearby tornado passage (1727 UTC). The black descending arrow denotes a deep layer of destabilization resulting from mid- to lower-tropospheric decreases in θ_e. Short black ascending arrow depicts rapid destabilization resulting from near-surface processes.

earlier ones). Also, a direct comparison of the hodographs from the profiler and vLAPS at the two earlier times (Figs. 14a–d) reveals very similar shapes throughout the 6-km depth of the atmosphere displayed. This general agreement further attests to the validity of our data merging technique.

These hodograph changes translate directly into important temporal changes in the computed SRH for each of several layers considered (Fig. 15). During the early morning period, the wind profiler and vLAPS both show small, negative values for the 0–1-km-layer SRH, gradually increasing to a maximum of 134 m^2 s^{-2} by 1745 UTC, a value in agreement with that determined from the Denver rawinsonde (Fig. 5). Much more dramatic SRH increases to maxima of 220 and 290 m^2 s^{-2} appear in the 0–3- and 0–6-km layers, respectively. The 0–3-km SRH is used in operations (Bunkers et al. 2006). The value of 220 exceeds the 150 m^2 s^{-2} value suggested by Davies-Jones et al. (1990) as being an approximate lower threshold for mesocyclone formation. The explanation for these large and rapid increases in helicity is that the growing depth and magnitude of the southeasterly wind regime resulted in a much larger positive area between the tip of the storm motion vector (158° at 17.5 m s^{-1}) and the hodograph curve over the respective layer depth. Positive SRH, which results when the storm motion vector lies to the right of the hodograph, equates

to streamwise horizontal vorticity, which is important because, when ingested by the storm updraft, the updraft acquires net cyclonic rotation (supercell character). The implication is that the rapid development of large, positive SRH after 1615 UTC produced an environment that was highly conducive to the formation of supercell storms. The increasing southeasterly wind regime was associated with the advance of the warm front through the Windsor CI region. Markowski et al. (1998) have noted the strong relationship between the occurrence of significant tornadoes and the presence of mesoscale low-level boundaries. They speculated that the horizontal vorticity generated at boundaries is an important vorticity source for low-level mesocyclones via tilting and stretching.

Differences in SRH do exist using the wind profiler and interpolated vLAPS analyses, although these differences are generally <100 m^2 s^{-2} and are associated with mostly negative SRH values prior to 1600 UTC, which is definitely not supportive of right-moving supercell environments and tornadogenesis. Nonetheless, it is interesting that the vLAPS values are, for the most part, systematically smaller than those obtained from the profiler. The reason for this is related to subtle details in the respective hodographs, resulting in the partial cancellation of the small positive areas to a relatively greater extent in the vLAPS hodographs. Markowski
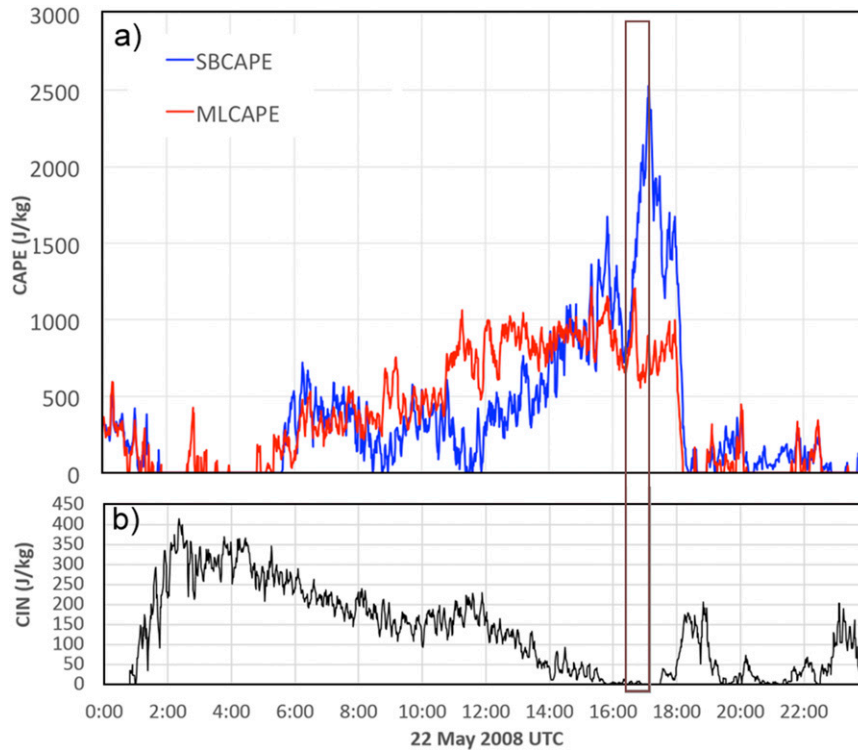
FIG. 12. Time series of (a) radiometer-derived 5-min-averaged SBCAPE (blue) and MLCAPE (red) and (b) CIN. The gray box highlights the 45-min period just before tornado passage (1727 UTC) during which SBCAPE increased suddenly to its maximum depicted value of $2550\,\mathrm{J\,kg^{-1}}$ in conjunction with CIN = 0. This is followed by a rapid decrease in both SBCAPE and MLCAPE after 1800 UTC in association with passage of the dryline. Actual peak value of SBCAPE from unfiltered data was $2886\,\mathrm{J\,kg^{-1}}$.

and Richardson (2010) discuss how small changes in hodograph geometry can result in sizable differences in SRH.

A time–height plot of vertical wind shear from the merged dataset shown in Fig. 16 provides insight into the influence of the ULJ passage on the development of high SRH over the Windsor CI region. Shear increased in the 1.5–2.8-km layer after 1600 UTC in association with a downward descent of the level of maximum shear from ~4.7 km at 1100 UTC to 1.5 km AGL during the development of the tornado. A highly significant consequence of this evolution was the increasing SRH in the lower troposphere and depth of strong vertical wind shear. As pointed out by Bunkers et al. (2006), the deep-layer shear is characteristically strong in long-lived supercell environments because it supports updraft intensification.

6. Conclusions

The combined availability of a microwave radiometer and a wind profiler in the immediate vicinity of a powerful tornado, in conjunction with a 1-km-resolution variational mesoanalysis/prediction system (vLAPS), provided observations with unprecedented detail showing extremely rapid changes in the near-storm environment for a very unusual tornado event. These ground-based profile data were assimilated into vLAPS, along with WSR-88D data and other conventional observations, even though an experiment performed omitting the profiler data in the vLAPS analysis system showed negligible impacts. This was not surprising given that data from only a single wind profiler was withdrawn, and for this reason, a comparable data sensitivity study denying the radiometer data was not conducted.

The radiometer provided excellent temporal and vertical continuity in retrieved water vapor mixing ratio, potential instability, and other thermodynamic variables to at least 5 km AGL. A pronounced surge in SBCAPE 45 min before tornado touchdown followed several hours of continuous, gradual increase in SBCAPE throughout the morning. The latter finding is similar to results obtained using a variety of ground-based remote sensing systems in previous severe storm case studies,
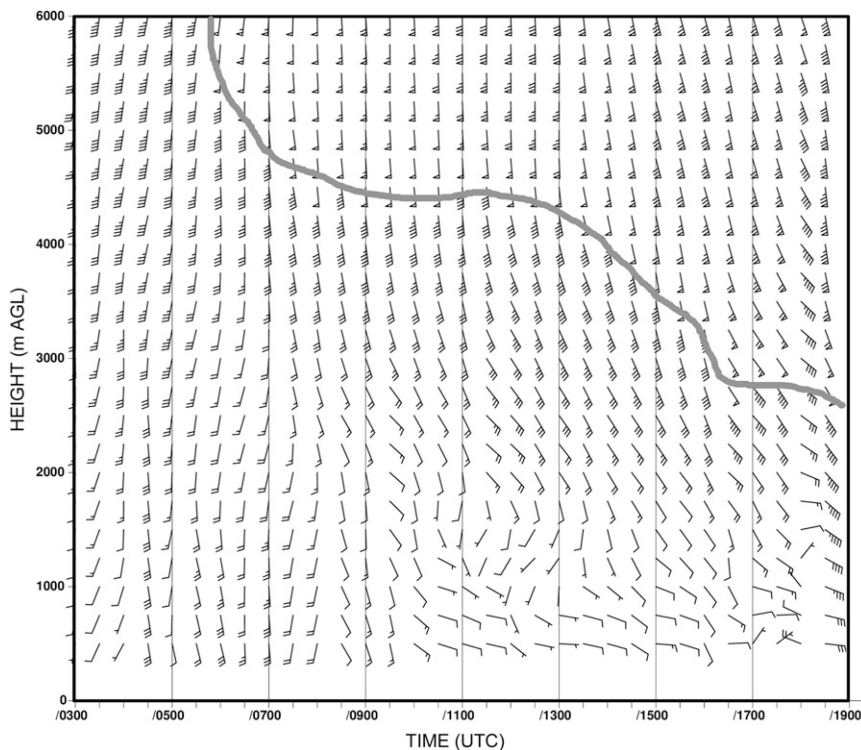
FIG. 13. Merged time–height plot of horizontal winds from combining objectively analyzed wind profiler data prior to 1600 UTC with winds (kt) from vLAPS afterward. All data have been reduced to 30-min intervals. Curve represents subjectively analyzed 50-kt isotach.

but the sudden surge in SBCAPE has, to our awareness, not been reported before. SBCAPE calculated from the radiometer reached a peak of $2866\,\mathrm{J\,kg^{-1}}$ just 20 min before the tornado formed and was associated with very strong and rapid destabilization in the lowest few hundred meters of the atmosphere.

Combined wind profiler–vLAPS analysis revealed that wind shear also rapidly increased just prior to tornado formation ~90 min prior to tornadogenesis, following several hours of descent of strong vertical wind shear initially in the upper troposphere down to 1.5 km AGL just before the tornado developed. Following several hours of negligible changes in storm-relative helicity, the SRH in the 0–3-km layer jumped from -100 to $220\,\mathrm{m^2\,s^{-2}}$ in the 1.5 h prior to tornado touchdown. Thus, rapid, shallow-layer destabilization worked in concert with impressive increases in deep vertical wind shear and SRH to create conditions highly conducive to the generation of this long-lived tornadic supercell in a region and at a time when such events rarely occur.

These rapidly evolving, near-storm environmental changes were interpreted within the framework of the mesoscale environment revealed in the vLAPS analyses. Diagnostics indicated a complex sequence of

scale-interactive processes were at play in producing an environment that could support strong tornadoes, beginning with the appearance of a very strong jet streak at 300 hPa and associated mass divergence, followed by mass and momentum adjustments in the lower troposphere associated with the ULJ dynamics. Those adjustments included significant acceleration of the low-level winds from a southeasterly direction, strengthening and westward retrogression of a pronounced surface low pressure system (Denver Cyclone) to the foothills region of the Colorado Rockies, warm frontogenesis immediately to its east, and the consequential north-westward advection of high moisture content, instability, and wind shear.

These results point to the tremendous value of the excellent temporal sampling provided by ground-based thermodynamic and wind profiler systems in cases of high-impact weather events. They suggest that rarely documented, extremely rapid destabilization, increasing moisture, and streamwise vorticity can occur, which are critical to the development of some kinds of tornado events. It is unfortunate that the NOAA 404-MHz wind profiler network has been discontinued, since aside from the WSR-88D velocity–azimuth profiles, forecasters have no routine access to detailed wind profile
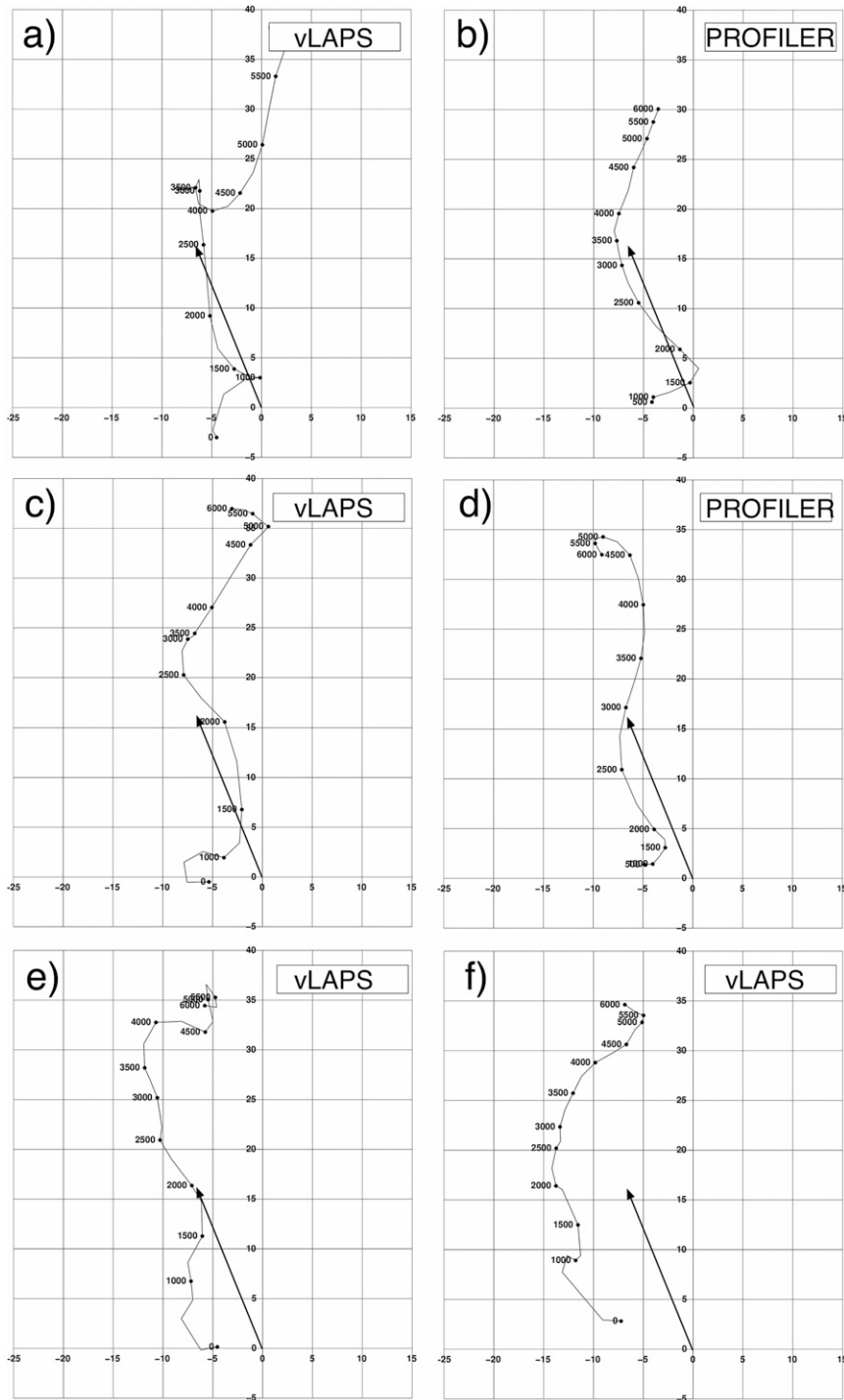
FIG. 14. Comparison of hodographs (m s^{-1}) obtained from vLAPS analysis at the grid point nearest to the Platteville wind profiler and the profiler at (a),(b) 1330 and (c),(d) 1530 UTC. The vLAPS-only hodographs are shown at (e) 1700 and (f) 1730 UTC. SRH in a layer (e.g., 0–6 km) is graphically equal to twice the area swept out from the tip of the storm motion vector (arrow) to the points on the hodograph over that layer. See text for further discussion of the meaning of SRH in this context.
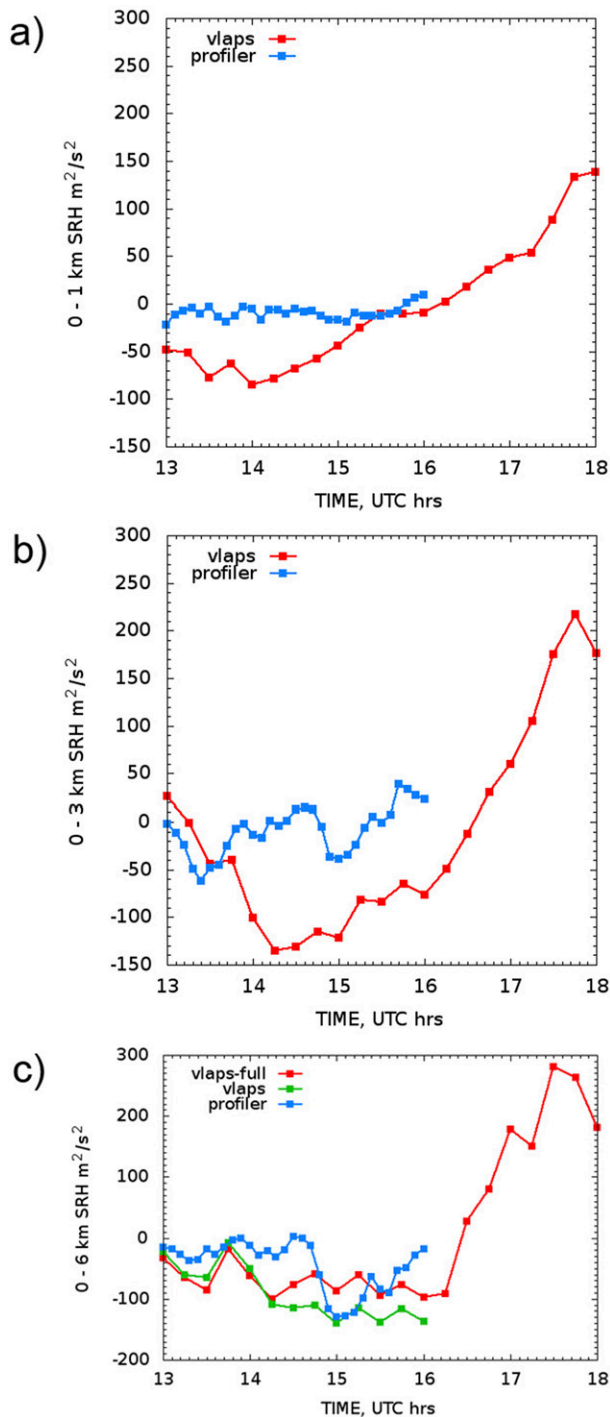
a)

b)

c)

FIG. 15. Time series of SRH ($m^2\,s^{-2}$) for (a) 0–1-, (b) 0–3-, and (c) 0–6-km layers from the wind profiler prior to 1600 UTC (blue), vLAPS (red), and a partial layer excluding the lowest 500 m AGL (green) from vLAPS for direct comparison with the profiler results since it did not produce data in the lowest 500 m.
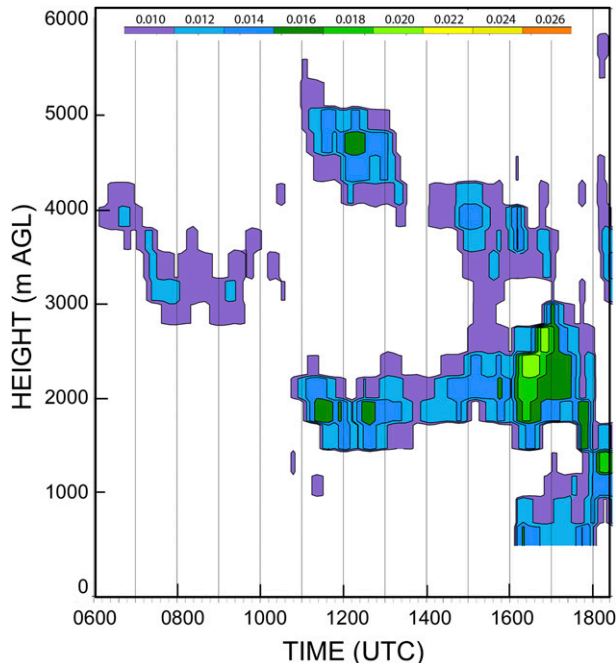

FIG. 16. Time–height plot of vertical wind shear (s^{-1}) from merged profiler–vLAPS winds for the period 0600–1830 UTC at 12-min intervals. Note the continuous descent of strong shear after 1300 UTC and a rapid increase in shear in the 2.0–2.5-km layer after 1600 UTC associated with the appearance of strong winds from a southeasterly direction (cf. Fig. 13).

information on the mesoscale or smaller. Neither does the weather community have in place a dense nationwide network of ground-based remote sensing systems or in situ sensors for monitoring rapid changes in the mesoscale thermodynamic state. More studies of this kind are unquestionably needed to gain a fuller understanding of the generality of our findings, either by finding past events when both kinds of observing systems happened to capture an interesting situation, or when special mesoscale field programs had established a dense network of remote sensing systems capable of capturing such rapid mesoscale changes.

REFERENCES

Albers, S., J. A. McGinley, D. L. Birkenheuer, and J. R. Smart, 1996: The Local Analysis and Prediction System (LAPS): Analyses of clouds, precipitation, and temperature. *Wea. Forecasting*, **11**, 273–287, doi:10.1175/1520-0434(1996)011<0273:TLAAPS>2.0.CO;2.

Atkins, N., R. Wakimoto, and C. Ziegler, 1998: Observations of the finescale structure of a dryline during VORTEX 95. *Mon. Wea. Rev.*, **126**, 525–550, doi:10.1175/1520-0493(1998)126<0525:OOTFSO>2.0.CO;2.

Benjamin, S. L., B. E. Schwartz, E. J. Szoke, and S. E. Koch, 2004: The value of wind profiler data in U.S. weather forecasting. *Bull. Amer. Meteor. Soc.*, **85**, 1871–1886, doi:10.1175/BAMS-85-12-1871.

Buban, M. S., C. L. Ziegler, E. N. Rasmussen, and Y. P. Richardson, 2007: The dryline on 22 May 2002 during IHOP: Ground-radar and in situ data analyses of the dryline and boundary layer evolution. *Mon. Wea. Rev.*, **135**, 2473–2505, doi:10.1175/MWR3453.1.

——, ——, E. R. Mansell, and Y. P. Richardson, 2012: Simulation of dryline misovortex dynamics and cumulus formation. *Mon. Wea. Rev.*, **140**, 3525–3551, doi:10.1175/MWR-D-11-00189.1.

Bunkers, M. J., J. S. Johnson, L. J. Czepyha, J. M. Grzywacz, and B. A. Klimowski, 2006: An observational examination of long-lived supercells. Part II: Environmental conditions and forecasting. *Wea. Forecasting*, **21**, 689–714, doi:10.1175/WAF952.1.

Campos, E. F., R. Ware, P. Joe, and D. Hudak, 2014: Monitoring water phase dynamics in winter clouds. *Atmos. Res.*, **147–148**, 86–100, doi:10.1016/j.atmosres.2014.03.008.

Chadwick, R. B., and N. Hassel, 1987: Profiler: The next generation surface-based atmospheric sounding system. Preprints, *Third Int. Conf. on Interactive Information and Processing Systems for Meteorology*, New Orleans, LA, Amer. Meteor. Soc., 15–21.

Cimini, D., T. J. Hewison, L. Martin, J. Güldner, C. Gaffard, and F. Marzano, 2006: Temperature and humidity profile retrievals from ground-based microwave radiometers during TUC. *Meteor. Z.*, **15**, 45–56, doi:10.1127/0941-2948/2006/0099.

——, and Coauthors, 2011: Thermodynamic atmospheric profiling during the 2010 Winter Olympics using ground-based microwave radiometry. *IEEE Trans. Geosci. Remote Sens.*, **49**, 4959–4969, doi:10.1109/TGRS.2011.2154337.

——, F. De Angelis, J. Dupont, S. Pal, and M. Haeffelin, 2013: Mixing layer height retrievals by multichannel microwave radiometer observations. *Atmos. Meas. Tech.*, **6**, 2941–2951, doi:10.5194/amt-6-2941-2013.

Craven, J. P., and H. E. Brooks, 2004: Baseline climatology of sounding derived parameters associated with deep, moist convection. *Natl. Wea. Dig.*, **28**, 13–24.

Dabberdt, W. F., and Coauthors, 2005: Multifunctional mesoscale observing networks. *Bull. Amer. Meteor. Soc.*, **86**, 961–982, doi:10.1175/BAMS-86-7-961.

Davies-Jones, R., D. Burgess, and M. Foster, 1990: Test of helicity as a tornado forecast parameter. Preprints, *16th Conf. on Severe Local Storms*, Kananaskis Park, AB, Canada, Amer. Meteor. Soc., 588–592.

Droegemeier, K. K., S. M. Lazarus, and R. Davies-Jones, 1993: The influence of helicity on numerically simulated convective storms. *Mon. Wea. Rev.*, **121**, 2005–2029, doi:10.1175/1520-0493(1993)121<2005:TIOHON>2.0.CO;2.

Feltz, W. F., and J. R. Mecikalski, 2002: Monitoring high-temporal-resolution convective stability indices using the ground-based Atmospheric Emitted Radiance Interferometer (AERI) during

the 3 May 1999 Oklahoma–Kansas tornado outbreak. *Wea. Forecasting*, **17**, 445–455, doi:10.1175/1520-0434(2002)017<0445:MHTRCS>2.0.CO;2.

Finch, J., and D. Bikos, 2010: A long-lived tornadic supercell over Colorado and Wyoming, 22 May 2008. *Electron. J. Severe Storms Meteor.*, **5** (5). [Available online at http://www.ejssm.org/ojs/index.php/ejssm/article/viewArticle/63.]

Geerts, B., T. Andretta, S. J. Luberda, J. Vogt, Y. Wang, and L. D. Oolman, 2009: A case study of a long-lived tornadic mesocyclone in a low-CAPE complex-terrain environment. *Electron. J. Severe Storms Meteor.*, **4** (3). [Available online at http://www.ejssm.org/ojs/index.php/ejssm/article/viewArticle/59.]

Güldner, J., 2013: A model-based approach to adjust microwave observations for operational applications: results of a campaign at Munich airport in winter 2011/2012. *Atmos. Meas. Tech.*, **6**, 2879–2891, doi:10.5194/amt-6-2879-2013.

——, and D. Spänkuch, 2001: Remote sensing of the thermodynamic state of the atmospheric boundary layer by ground-based microwave radiometry. *J. Atmos. Oceanic Technol.*, **18**, 925–933, doi:10.1175/1520-0426(2001)018<0925:RSOTTS>2.0.CO;2.

Hardesty, R. M., and Coauthors, 2012: Thermodynamic Profiling Technologies Workshop report to the National Science Foundation and the National Weather Service. NCAR Tech. Note NCAR/TN-488+STR, 80 pp., doi:10.5065/D6SQ8XCF.

Hartung, D. C., J. A. Otkin, R. A. Petersen, D. D. Turner, and W. F. Feltz, 2011: Assimilation of surface-based boundary layer profiler observations during a cool-season weather event using an observing system simulation experiment. Part II: Forecast assessment. *Mon. Wea. Rev.*, **139**, 2327–2346, doi:10.1175/2011MWR3623.1.

Hewison, T., 2007: 1D-VAR retrieval of temperature and humidity profiles from a ground-based microwave radiometer. *IEEE Trans. Geosci. Remote Sens.*, **45**, 2163–2168, doi:10.1109/TGRS.2007.898091.

Hiemstra, C. A., G. E. Liston, R. A. Pielke, D. L. Birkenheuer, and S. C. Albers, 2006: Comparing Local Analysis and Prediction System (LAPS) assimilations with independent observations. *Wea. Forecasting*, **21**, 1024–1040, doi:10.1175/WAF961.1.

Illingworth, A., D. Cimini, C. Gaffard, M. Haeffelin, V. Lehmann, U. Löhnert, E. O'Connor, and D. Ruffieux, 2015: Exploiting existing ground-based remote sensing networks to improve high resolution weather forecasts. *Bull. Amer. Meteor. Soc.*, **96**, 2107–2125, doi:10.1175/BAMS-D-13-00283.1.

Jiang, H., and Coauthors, 2015: Real-time applications of the variational version of the Local Analysis and Prediction System (vLAPS). *Bull. Amer. Meteor. Soc.*, **96**, 2045–2057, doi:10.1175/BAMS-D-13-00185.1.

Knupp, K., T. R. Coleman, D. Phillips, R. Ware, D. Cimini, F. Vandenberghe, J. Vivekanandan, and E. Westwater, 2009: Ground-based passive microwave profiling during dynamic weather conditions. *J. Atmos. Oceanic Technol.*, **26**, 1057–1073, doi:10.1175/2008JTECHA1150.1.

Koch, S. E., and J. McCarthy, 1982: The evolution of an Oklahoma dryline. Part II: Boundary-layer forcing of mesoconvective systems. *J. Atmos. Sci.*, **39**, 237–257, doi:10.1175/1520-0469(1982)039<0237:TEOAOD>2.0.CO;2.

——, and W. L. Clark, 1999: A nonclassical cold front observed during COPS-91: Frontal structure and the process of severe storm initiation. *J. Atmos. Sci.*, **56**, 2862–2890, doi:10.1175/1520-0469(1999)056<2862:ANCFOD>2.0.CO;2.

——, M. desJardins, and P. J. Kocin, 1983: An interactive Barnes objective map analysis scheme for use with satellite and

conventional data. *J. Climate Appl. Meteor.*, **22**, 1487–1503, doi:10.1175/1520-0450(1983)022<1487:AIBOMA>2.0.CO;2.

Liljegren, J., S. Boukabara, K. Cady-Pereira, and S. Clough, 2004: The effect of the half-width of the 22-GHz water vapor line on retrievals of temperature and water vapor profiles with a 12-channel microwave radiometer. *IEEE Trans. Geosci. Remote Sens.*, **43**, 1102–1108, doi:10.1109/TGRS.2004.839593.

Madhulatha, A., M. Rajeevan, M. Venkat Ratnam, J. Bhate, and C. V. Naidu, 2013: Nowcasting severe convective activity over southeast India using ground-based microwave radiometer observations. *J. Geophys. Res.*, **118**, 1–13, doi:10.1029/2012JD018174.

Markowski, P. M., E. N. Rasmussen, and J. M. Straka, 1998: The occurrence of tornadoes in supercells interacting with boundaries during VORTEX-95. *Wea. Forecasting*, **13**, 852–859, doi:10.1175/1520-0434(1998)013<0852:TOOTIS>2.0.CO;2.

——, and Y. Richardson, 2010: *Mesoscale Meteorology in Midlatitudes*. Wiley-Blackwell, 407 pp.

McCarthy, J., and S. E. Koch, 1982: The evolution of an Oklahoma dryline. Part I: A mesoscale and subsynoptic-scale analysis. *J. Atmos. Sci.*, **39**, 225–236, doi:10.1175/1520-0469(1982)039<0225:TEOAOD>2.0.CO;2.

National Research Council, 2009: *Observing Weather and Climate from the Ground Up: A Nationwide Network of Networks*. National Academies Press, 234 pp.

——, 2010: *When Weather Matters: Science and Service to Meet Critical Societal Needs*. National Academies Press, 181 pp.

Otkin, J. A., D. C. Hartung, D. D. Turner, R. A. Petersen, W. F. Feltz, and E. Janzon, 2011: Assimilation of surface-based boundary layer profiler observations during a cool-season weather event using an observing system simulation experiment. Part I: Analysis impact. *Mon. Wea. Rev.*, **139**, 2309–2326, doi:10.1175/2011MWR3622.1.

Potvin, C. K., K. L. Elmore, and S. J. Weiss, 2010: Assessing the impacts of proximity sounding criteria on the climatology of significant tornado environments. *Wea. Forecasting*, **25**, 921–930, doi:10.1175/2010WAF2222368.1.

Rasmussen, E. N., 2003: Refined supercell and tornado forecast parameters. *Wea. Forecasting*, **18**, 530–535, doi:10.1175/1520-0434(2003)18<530:RSATFP>2.0.CO;2.

——, and D. O. Blanchard, 1998: A baseline climatology of sounding-derived supercell and tornado forecast parameters. *Wea. Forecasting*, **13**, 1148–1164, doi:10.1175/1520-0434(1998)013<1148:ABCOSD>2.0.CO;2.

Ratnam, M. V., Y. D. Santhi, M. Rajeevan, and S. V. Bhaskara Rao, 2013: Diurnal variability of stability indices observed using radiosonde observations over a tropical station: Comparison with microwave radiometer measurements. *Atmos. Res.*, **124**, 21–33, doi:10.1016/j.atmosres.2012.12.007.

Schumacher, R. S., D. T. Lindsey, A. B. Schumacher, J. Braun, S. D. Miller, and J. L. Demuth, 2010: Multidisciplinary analysis of an unusual tornado: Meteorology, climatology, and the communication and interpretation of warnings. *Wea. Forecasting*, **25**, 1412–1429, doi:10.1175/2010WAF2222396.1.

Serke, D., and Coauthors, 2014: Supercooled liquid water content profiling case studies with a new vibrating wire sonde compared to a ground-based microwave radiometer. *Atmos. Res.*, **149**, 77–87, doi:10.1016/j.atmosres.2014.05.026.

Solheim, F., J. Godwin, E. Westwater, Y. Han, S. Keihm, K. Marsh, and R. Ware, 1998: Radiometric profiling of temperature, water vapor, and cloud liquid water using various inversion methods. *Radio Sci.*, **33**, 393–404, doi:10.1029/97RS03656.

Szoke, E. J., M. L. Weisman, J. M. Brown, F. Caracena, and T. W. Schlatter, 1984: A subsynoptic analysis of the Denver tornadoes of 3 June 1981. *Mon. Wea. Rev.*, **112**, 790–808, doi:10.1175/1520-0493(1984)112<0790:ASAOTD>2.0.CO;2.

Thompson, R. L., and R. Edwards, 2000: An overview of environmental conditions and forecast implications of the 3 May 1999 tornado outbreak. *Wea. Forecasting*, **15**, 682–699, doi:10.1175/1520-0434(2000)015<0682:AOOECA>2.0.CO;2.

——, ——, J. A. Hart, K. L. Elmore, and P. Markowski, 2003: Close proximity soundings within supercell environments obtained from the Rapid Update Cycle. *Wea. Forecasting*, **18**, 1243–1261, doi:10.1175/1520-0434(2003)018<1243:CPSWSE>2.0.CO;2.

——, B. T. Smith, A. R. Dean, and P. T. Marsh, 2013: Spatial distributions of tornadic near-storm environments by convective mode. *Electron. J. Severe Storms Meteor.*, **8** (5). [Available online at http://www.ejssm.org/ojs/index.php/ejssm/issue/view/47.]

Trexler, C. M., and S. E. Koch, 2000: The life cycle of a mesoscale gravity wave as observed by a network of Doppler wind profilers. *Mon. Wea. Rev.*, **128**, 2423–2446, doi:10.1175/1520-0493(2000)128<2423:TLCOAM>2.0.CO;2.

Wagner, T. J., W. F. Feltz, and S. A. Ackerman, 2008: The temporal evolution of convective indices in storm-producing environments. *Wea. Forecasting*, **23**, 786–794, doi:10.1175/2008WAF2007046.1.

Wakimoto, R. M., H. V. Murphey, E. V. Browell, and S. Ismail, 2006: The "triple point" on 24 May 2002 during IHOP. Part I: Airborne Doppler and LASE analyses of the frontal boundaries and convection initiation. *Mon. Wea. Rev.*, **134**, 231–250, doi:10.1175/MWR3066.1.

Ware, R., R. Carpenter, J. Güldner, J. Liljegren, T. Nehrkorn, F. Solheim, and F. Vandenberghe, 2003: A multichannel radiometric profiler of temperature, humidity, and cloud liquid. *Radio Sci.*, **38**, 8079, doi:10.1029/2002RS002856.

——, and Coauthors, 2013: Thermodynamic and liquid profiling during the 2010 Winter Olympics. *Atmos. Res.*, **132–133**, 278–290, doi:10.1016/j.atmosres.2013.05.019.

Weckwerth, T. M., and D. B. Parsons, 2004: A review of convection initiation and motivation for IHOP_2002. *Mon. Wea. Rev.*, **134**, 5–22, doi:10.1175/MWR3067.1.

Weisman, M. L., and J. B. Klemp, 1982: The dependence of numerically simulated convective storms on vertical wind shear and buoyancy. *Mon. Wea. Rev.*, **110**, 504–520, doi:10.1175/1520-0493(1982)110<0504:TDONSC>2.0.CO;2.

——, and R. Rotunno, 2000: The use of vertical wind shear versus helicity in interpreting supercell dynamics. *J. Atmos. Sci.*, **57**, 1452–1472, doi:10.1175/1520-0469(2000)057<1452:TUOVWS>2.0.CO;2.

Weiss, C. C., and H. B. Bluestein, 2002: Airborne pseudo-dual-Doppler analysis of a dryline–outflow boundary intersection. *Mon. Wea. Rev.*, **130**, 1207–1226, doi:10.1175/1520-0493(2002)130<1207:APDDAO>2.0.CO;2.

Westwater, E., S. Crewell, C. Mäztler, and D. Cimini, 2005: Principles of surface-based microwave and millimeter wave radiometric remote sensing of the troposphere. *Quad. Soc. Ital. Elettromag.*, **1**, 50–84.

Wilson, J. W., N. A. Crook, C. K. Mueller, J. Sun, and M. Dixon, 1998: Nowcasting thunderstorms: A status report. *Bull. Amer. Meteor. Soc.*, **79**, 2079–2100, doi:10.1175/1520-0477(1998)079<2079:NTASR>2.0.CO;2.

WMO, 2010: *Guide to Meteorological Instruments and Methods of Observation*. 7th ed. WMO-No. 8, 681 pp. [Available

online at https://www.wmo.int/pages/prog/gcos/documents/gruanmanuals/CIMO/CIMO_Guide-7th_Edition-2008.pdf.]

Xie, Y., S. Koch, J. McGinley, S. Albers, P. E. Bieringer, M. Wolfson, and M. Chan, 2011: A space–time multiscale analysis system: A sequential variational analysis approach. *Mon. Wea. Rev.*, **139**, 1224–1240, doi:10.1175/2010MWR3338.1.

Xu, G., R. Ware, W. Zhang, G. Feng, K. Liao, and Y. Liu, 2014: Effect of off-zenith observations on reducing the impact of precipitation on ground-based microwave radiometer measurement accuracy. *Atmos. Res.*, **140–141**, 85–94, doi:10.1016/j.atmosres.2014.01.021.

Ziegler, C., W. Martin, R. Pielke, and R. Walko, 1995: A modeling study of the dryline. *J. Atmos. Sci.*, **52**, 263–285, doi:10.1175/1520-0469(1995)052<0263:AMSOTD>2.0.CO;2.

——, E. R. Mansell, J. M. Straka, D. R. MacGorman, and D. W. Burgess, 2010: The impact of spatial variations of low-level stability on the life cycle of a simulated supercell storm. *Mon. Wea. Rev.*, **138**, 1738–1766, doi:10.1175/2009MWR3010.1.